

RIS-Enabled and Access-Point-Free Simultaneous Radio Localization and Mapping

Hyowon Kim, *Member, IEEE*, Hui Chen, *Member, IEEE*,

Musa Furkan Keskin, *Member, IEEE*, Yu Ge, *Student Member, IEEE*,

Kamran Keykhosravi, *Member, IEEE*, George C. Alexandropoulos, *Senior*

Member, IEEE, Sunwoo Kim, *Senior Member, IEEE*, and

Henk Wymeersch, *Senior Member, IEEE*

Abstract

In the upcoming sixth generation (6G) of wireless communication systems, reconfigurable intelligent surfaces (RISs) are regarded as one of the promising technological enablers, which can provide programmable signal propagation. Therefore, simultaneous radio localization and mapping (SLAM) with RISs appears as an emerging research direction within the 6G ecosystem. In this paper, we propose a novel framework of RIS-enabled radio SLAM for wireless operation without the intervention of access points (APs). We first design the RIS phase profiles leveraging prior information for the user equipment (UE), such that they uniformly illuminate the angular sector where the UE is probabilistically located. Second, we modify the marginal Poisson multi-Bernoulli SLAM filter and estimate the UE state and landmarks, which enables efficient mapping of the radio propagation environment. Third, we derive the theoretical Cramér-Rao lower bounds on the estimators for the channel parameters and the UE state. We finally evaluate the performance of the proposed method under scenarios with a limited number of transmissions, taking into account the channel coherence time. Our results demonstrate that the RIS

H. Kim, H. Chen, M. F. Keskin, Y. Ge, and H. Wymeersch are with the Department of Electrical Engineering, Chalmers University of Technology, 412 58 Gothenburg, Sweden (emails: {hyowon, hui.chen, furkan, yuge, henkw}@chalmers.se).

K. Keykhosravi is with Ericsson Research, Ericsson AB, Gothenburg, Sweden (e-mail:kamran.keykhosravi@ericsson.com).

G. C. Alexandropoulos is with the Department of Informatics and Telecommunications, National and Kapodistrian University of Athens, 15784 Athens, Greece (e-mail: alexandg@di.uoa.gr).

S. Kim is with the Department of Electronic Engineering, Hanyang University, 04763 Seoul, South Korea (email: remero@hanyang.ac.kr).

This work was supported in part by the EU H2020 RISE-6G project under grant 101017011, the Chalmers Area of Advance Transport 6G-Cities project, and Basic Science Research Program through the National Research Foundation of Korea (2022R1A6A3A03068510).

enables solving the radio SLAM problem with zero APs, and that the consideration of the Doppler shift contributes to improving the UE speed estimates.

Index Terms

Doppler shift, localization, mapping, phase profile design, reconfigurable intelligent surface, 6G, Poisson multi-Bernoulli, SLAM.

I. INTRODUCTION

Simultaneous localization and mapping (SLAM) has been a highly active research topic in wireless communications [1]–[9] as well as in robotics [10], [11]. According to the late advances in wireless systems design, spatial information has been attracting attention in location-aware communications [12], [13] for fifth generation (5G) systems, as well as in integrated sensing and communications (ISAC) [14]–[16], a concept intended for beyond 5G and sixth generation (6G). In 5G, large bandwidths and multiple antennas are considered at millimeter-wave (mmWave) carrier frequencies, hence, high-resolvable time-of-arrival (ToA), angle-of-departure (AoD), and angle-of-arrival (AoA) for each resolvable signal propagation path are feasible [4], [17]. This has been lately motivating various studies on radio SLAM [1]–[9].

In line with the 5G developments, radio SLAM methods have been devised [1]–[9], enabling estimating the user equipment (UE) state while simultaneously mapping the landmarks in the propagation environment. In [1]–[3], random finite sets (RFSs) were adopted for modeling the unknown position and number of landmarks, as well as the uncertain data association between landmarks and measurements with missed detections and false alarms. Depending on the case-by-case scenario, we approximate the RFS density for modeling a set of landmarks and can utilize the desired RFS. By avoiding the assignment problem for data association, the trade-off between the performance and computational complexity was balanced in [1]. An efficient implementation using the extended Kalman filter was developed in [2], by computing the marginalized SLAM density together with data association. From the RFS-SLAM density, which can handle the SLAM problem in a theoretically optimal manner, a series of SLAM densities was derived by marginalizing out either multiple hypotheses or nuisance variables [3]. This implementation was computationally efficient and its connection to the belief propagation (BP)-based SLAM filter was showcased [6]. In BP-SLAM [4]–[7], the landmark position was modeled by a vector, and the marginalized densities, corresponding to individual UE state and landmarks, were computed

via BP. With the known number of landmarks, the SLAM problem was formulated as a factor graph [4], [5] and multiple types of landmarks were considered in [5]. For the case of unknown number of landmarks, the factor graph including data association was proposed in [6], and the authors in [7] additionally considered the clock bias in the UE state estimation problem. Non-Bayesian methods using geometry relations were recently studied in [8], [9]. Considering known number of landmarks and data association, the SLAM problem was formulated and solved in [8]. The authors in [9] considered a single base station (BS) with an unknown position to the SLAM system.

Complementary to SLAM, ISAC and reconfigurable intelligent surfaces (RISs) have recently emerged as very promising technologies for the future 6G wireless communications, providing the necessary measurement data for high-precision SLAM. ISAC is recently attracting increasing attention according to which, sensing and communication functionalities can be delivered simultaneously in a given propagation environment [14]–[16], while RISs [18], [19] can offer programmable signal propagation [20], enabling various wireless applications [21]. For example, RISs have been proposed as a new paradigm in radio localization [22], [23], rendering location estimation feasible even in cases where it is not with conventional nodes [24]. Leveraging its radio propagation control capability, an RIS can provide a reference point with reliable geometric measurements, generating the desired signal path and power. In a single-input single-output (SISO) system, channel parameter estimation and the Cramér-Rao lower bounds (CRLB) on the UE state estimation were studied in [25]. The CRLBs on the position and heading¹ were derived in a multiple-input multiple-output (MIMO) system in [26], and localization with an array-of-subarray-based THz systems was discussed in [27]. The authors in [28] considered a blocked line-of-sight (LOS) path and studied RIS-aided localization, and furthermore, user localization and AoA estimation were simultaneously addressed for MIMO systems [29]. Without a BS, self-localization was proposed in an RIS-equipped SISO wireless system in [30]. In sensing and radar applications aided by reflective RISs, the receiver side was used to sense the signal reflected by the RIS elements, which enabled coverage extension [31] and signal-to-noise ratio (SNR) enhancement [32]. The unknown RIS position and orientation were addressed by bistatic sensing in [33]. Considering the RIS-aided sensing and localization together, several SLAM cases were introduced in [23], and a SLAM algorithm was developed for the case where multiple RISs are

¹The heading is the direction of the agent facing in the angular domain, also known as orientation.

considered as the unknown controllable passive objects [34]. In joint radar and communication systems, RIS-aided sensing helped to improve the performance of radar detection and alleviate mutual interference [35]. Very recently, various applications and benefits of RISs for sensing functionalities and for ISAC systems were discussed [16]. However, in spite of the latter RIS-based advantages, signals reaching a passive object via and RIS suffer from severe path loss.

The RIS capability to adjust the phase shifts of its individual elements provides additional degrees of freedom that can boost the localization performance in RIS-aided wireless systems [22]. In [36], [37], heuristic designs of directional RIS phase profiles were presented with the objective of SNR maximization in the presence of prior knowledge about the UE location. Localization-optimal designs via the CRLB minimization for a single-antenna receiver were studied in [38], leading to considerable accuracy improvements over standard directional and discrete Fourier transform (DFT)-based phase profiles, at a cost of increased transmission delays. To generate the arbitrary beampatterns, RIS configuration optimization was introduced in [39]. For multi-objects sensing using the round-trip signals via the RIS, the RIS configurations and beamforming vectors were jointly designed in [40]. The authors in [41] considered the UE position for RIS-based illumination, with the goal to reduce the RIS reconfiguration overhead, offering a large illumination area. To reduce the beam training overhead while sustaining the beam's quality, a hierarchical RIS phase profile design was devised in [42]. In [25], the Doppler effect, induced by mobility in various relevant applications, was considered [43]. While the impacts of this effect and its exploitation have been extensively studied in the context of traditional localization [44]–[46], it has received only limited treatment in RIS-aided localization. In the absence of prior information about the UE state, random phase configurations (either random element phases or random directions) can be employed [25], [28], providing an SNR gain over time. Moreover, temporal RIS phase coding offers an extra degree of freedom that allows for the separation of controlled (i.e., through the RIS) and uncontrolled paths (i.e., due to other reflectors and scatterers in the signal propagation environment) [25], [28], thereby facilitating subsequent processing. In RIS-enabled SLAM, sensing is carried out by the UE, while the RIS contributes in the estimation of the UE state, and only indirectly improves the mapping/sensing performance [22].

In this paper, we extend the RIS-enabled localization concept of [30], intended for cases of absence of BSs, to SLAM, considering that the full-duplex UE [47] transmits orthogonal frequency-division multiplexing (OFDM) signals and receives their back-scattered versions from the wireless propagation environment, as shown in Fig. 1. To the best of our knowledge, this

is the first study of RIS-enabled SLAM with zero BSs. In contrast to our recent work [30], we map the landmarks in the environment and use this mapping to improve UE localization. The contributions of this paper are summarized as follows.

- **RIS-aided SLAM modeling:** We propose a novel SLAM problem, where a full-duplex UE localizes itself with aid of an RIS and simultaneously maps objects in the environment, all based on single-bounce paths. In contrast to [34], a channel model for OFDM-MIMO systems is considered which accounts for the RIS via the AoA/AoD to/from it, the Doppler shift induced by mobility, and the random phase offset due to signal reflections.
- **Efficient RIS phase profile design:** To optimize SLAM performance, we present adaptive RIS phase profiles that take into account prior information on the UE location and enable uniform illumination of the corresponding angular uncertainty region, while being flexible with the number of transmission slots and targeted coverage probability. In contrast to [42], the angular uncertainty region is computed using UE prior information over consecutive time steps. Specifically, the region is divided into multiple grids depending on the number of transmissions, and each grid is covered by the proposed beam per transmission slot.
- **RFS-based SLAM filter extension:** We present an extension of the marginal Poisson multi-Bernoulli (MPMB)-SLAM filter from the recent work [3], which is capable to separate the reflected signal induced by the RIS from multipath signals, thus, facilitating the determination of landmarks in a global coordinate system.
- **Performance evaluation:** We verify via numerical simulations that the proposed RIS-enabled SLAM approach, together with the designed adaptive RIS phase profiles, provides satisfactory performance even when small numbers of transmissions are used (due to, for example, channel coherence time limitations), outperforming the conventional random and directional phase profiles. We also incorporate the Doppler shift into our channel model to address UE mobility scenarios, and it is shown that this significantly improves the SLAM performance through providing accurate UE speed estimation.

The remainder of this paper is organized as follows. Section II describes the various models for our RIS-enabled SLAM. The proposed RIS phase profile design is presented in Section III, while, in Section B, we derive the Fisher information matrix (FIMs) of the channel parameters and UE state. The proposed MPMB-SLAM filter for sequential Bayesian estimation is presented in Section IV. Our framework's extensive numerical investigations are discussed in Section V,

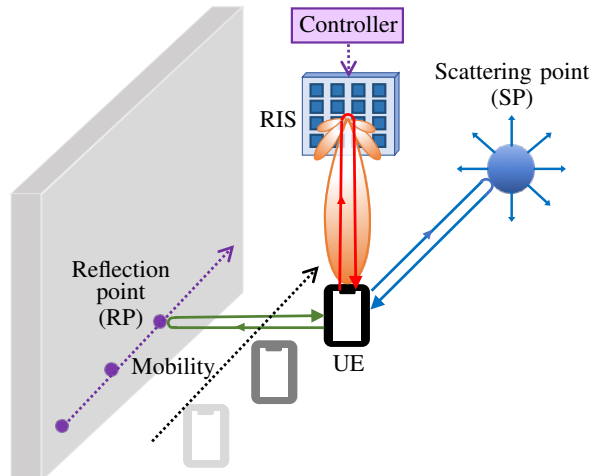


Fig. 1: An example illustration of the considered RIS-enabled radio SLAM setup that does not require the presence of a BS or access point. The full-duplex UE uses the RIS to localize itself and to place detected landmarks in the global frame of reference.

while Section VI concludes the paper.

Notation: The scalars, vectors, matrices, and sets are respectively represented by italic, bold lowercase, bold uppercase, and calligraphic fonts (e.g., x , \mathbf{x} , \mathbf{X} , and \mathcal{X}). The transpose and Hermitian of vectors and matrices are respectively expressed by the superscripts \top and H (e.g., \mathbf{x}^\top , \mathbf{X}^\top , \mathbf{X}^H). In addition, \odot denotes the Hadamard product, $\text{Re}(\cdot)$ is the real part of a complex value, $\|\cdot\|$ returns the Euclidean distance, and $|\cdot|$ provides the amplitude of a complex number. We use the following indices: antenna element n ; discrete time instant k ; transmission interval t ; subcarrier number s ; landmark i ; landmark type m ; measurement j ; and signal path l .

II. CONSIDERED MODELS AND DESIGN

This section introduces the focused wireless signal propagation environment and presents the considered models for the received signal and channel, as well as our measurements' models.

A. Signal and Channel Models

As shown in Fig. 1, we consider wireless signal propagation environments, where there is no BS.² The full-duplex UE moves and transmits mmWave signals, and multipath components are generated depending on the considered propagation environment as follows: *i*) reflected by the RIS elements, resulting in phase shifted versions of the impinging signals at the RIS (UE-RIS-UE path); *ii*) reflected by the reflection points (RPs) on the large surface (LS) (such as a

²It is noted that a BS may still be present in the scenario to coordinate the transmissions, but it is not directly involved in the SLAM signals or processing thereof.

wall), indicating specular reflection [4]–[7] (UE-RP-UE path); and *iii*) scattered by the scattering points (SPs) (UE-SP-UE path). During the same time-frequency resources, the UE receives the back-propagated signals. Note that we consider only the one-bounce signal propagation [1], [3], [6], consisting of $L + 1$ paths (L landmarks and 1 RIS); signals resulting from multiple bounces are considered as highly attenuated. The UE and RIS are respectively equipped with $N_{\text{UE}} = N_{\text{UE}}^{\text{az}} \times N_{\text{UE}}^{\text{el}}$ and $N_{\text{RIS}} = N_{\text{RIS}}^{\text{az}} \times N_{\text{RIS}}^{\text{el}}$ radiating elements (in the azimuth and elevation) forming uniform planar arrays (UPAs). The UE transmits at discrete time intervals k , with period Δ , T OFDM pilot symbols spanning N_{SC} subcarriers. We model the received signal on the s -th subcarrier for each t -th transmission as follows:

$$y_{t,k,s} \triangleq \sqrt{E_s} \mathbf{w}_{t,k}^H \sum_{l=0}^L \gamma_{l,k} \beta_{l,k} e^{j2\pi(f_{l,k}^{\text{D}} T_o t - \tau_{l,k}(s-1)\Delta_f)} \mathbf{a}_{\text{UE}}(\boldsymbol{\theta}_{l,k}) \mathbf{a}_{\text{UE}}^{\top}(\boldsymbol{\theta}_{l,k}) \mathbf{f}_{t,k} + n_{t,k,s}, \quad (1)$$

where $\gamma_{0,k} = \mathbf{a}_{\text{RIS}}^{\top}(\boldsymbol{\phi}_k) \boldsymbol{\Omega}_{\text{RIS},t,k} \mathbf{a}_{\text{RIS}}(\boldsymbol{\phi}_k)$ and $\gamma_{l,k} = 1$ for $l > 0$, in which we denote by l the path index and define the RIS path for $l = 0$ (UE-RIS-UE) and the non-RIS (NRIS) paths with $l \neq 0$ (UE-RP-UE or UE-SP-UE). Moreover, E_s denotes the energy per each pilot symbol, $\mathbf{a}_{\text{RIS}}(\boldsymbol{\phi}_k)$ and $\mathbf{a}_{\text{UE}}(\boldsymbol{\theta}_k)$ are the response vectors for both AoD and AoA at the RIS and UE (defined in both azimuth and elevation, e.g., $\boldsymbol{\phi}_k \triangleq [\phi_k^{\text{az}}, \phi_k^{\text{el}}]^{\top}$ for path $l = 0$ and $\boldsymbol{\theta}_{l,k} \triangleq [\theta_{l,k}^{\text{az}}, \theta_{l,k}^{\text{el}}]^{\top}$ for any path l), $f_{l,k}^{\text{D}}$ is the Doppler, $\tau_{l,k}$ is the ToA, and $\beta_{l,k}$ is the complex path gain, all of the l -th path. In addition, $\mathbf{w}_{t,k} \in \mathbb{C}^{N_{\text{BS}} \times 1}$ denotes the analog combining vector at the UE receiver, $\mathbf{f}_{t,k} \in \mathbb{C}^{N_{\text{BS}} \times 1}$ is the precoding vector at the UE transmitter, and $n_{t,k,s} \sim \mathcal{CN}(0, \sigma_{\text{N}}^2)$ is the additive white Gaussian noise (AWGN) with noise variance σ_{N}^2 . Finally, $T_o = T_S + T_{\text{CP}}$ denotes the signal duration, Δ_f is the subcarrier spacing, $T_S = 1/\Delta_f$ is the symbol duration, and $T_{\text{CP}} = N_{\text{CP}}/B$ is the cyclic prefix (CP) duration with $N_{\text{CP}} = N_{\text{SC}} \epsilon_{\text{CP}}$ representing the number of CP subcarriers, B is the signal bandwidth with N_{SC} being the number of subcarriers, and ϵ_{CP} is the CP overhead. Finally, $\lambda = c/f_c$ is the wavelength where c is the speed of light and f_c is the carrier frequency.

The array response vectors $\mathbf{a}_{\text{RIS}}(\cdot)$ and $\mathbf{a}_{\text{UE}}(\cdot)$ are defined generically as follows:

$$\mathbf{a}_{\star}(\boldsymbol{\vartheta}) = \exp(j\check{\mathbf{X}}_{\star}^{\top} \mathbf{g}(\boldsymbol{\vartheta})), \quad (2)$$

where \star denotes the device type where antennas are mounted (e.g., \star is UE or RIS), notation $\boldsymbol{\vartheta} \triangleq [\vartheta^{\text{az}}, \vartheta^{\text{el}}]^{\top}$ represents the angular parameter vector corresponding to the array vector, $\check{\mathbf{X}}_{\star}$ is the antenna element locations of device \star in its local coordinate system (defined next in Section II-B), and $\mathbf{g}(\cdot)$ is the wavenumber vector given by $\mathbf{g}(\boldsymbol{\vartheta}) \triangleq \frac{2\pi}{\lambda} [\cos(\vartheta^{\text{az}}) \sin(\vartheta^{\text{el}}), \sin(\vartheta^{\text{az}}) \sin(\vartheta^{\text{el}}), \cos(\vartheta^{\text{el}})]^{\top}$.

For the RIS, $\mathbf{\Omega}_{\text{RIS},t,k} \triangleq \text{diag}(\boldsymbol{\omega}_{t,k})$, where $\boldsymbol{\omega}_{t,k} \in \mathbb{C}^{N_{\text{RIS}} \times 1}$ is the RIS phase profile with elements constrained to lie on the unit circle. We further define the following vector:

$$\mathbf{b}(\boldsymbol{\phi}_k) \triangleq \mathbf{a}_{\text{RIS}}(\boldsymbol{\phi}_k) \odot \mathbf{a}_{\text{RIS}}(\boldsymbol{\phi}_k) = \exp(2j\check{\mathbf{X}}_{\text{RIS}}^{\top} \mathbf{g}(\boldsymbol{\phi}_k)), \quad (3)$$

where \odot denotes the Hadamard product, and hence, the RIS part in (1) can be simplified as:

$$\mathbf{a}_{\text{RIS}}^{\top}(\boldsymbol{\phi}_k) \mathbf{\Omega}_{\text{RIS},t,k} \mathbf{a}_{\text{RIS}}(\boldsymbol{\phi}_k) = \boldsymbol{\omega}_{t,k}^{\top} \mathbf{b}(\boldsymbol{\phi}_k). \quad (4)$$

Note that the spacing between the nearest radiating elements at the UE and RIS are respectively $\lambda/2$ and $\lambda/4$ for addressing the grating lobes, due to the combined response $\mathbf{b}(\boldsymbol{\phi}_k)$ [30].

B. Geometrical Representations

Apart from the UE, we regard the RIS, SPs, and RPs as landmarks in this paper. The UE state, SP positions, and RP positions are assumed unknown, whereas we consider that the RIS position and orientation are known. The numbers of SPs and RPs are a priori unknown. We represent the UE state with the polar velocity and known constant turn [48], denoted by $\mathbf{s}_k \triangleq [\mathbf{x}_{\text{UE},k}^{\top}, \alpha_{\text{UE},k}, v_{\text{UE},k}]^{\top}$, where $\mathbf{x}_{\text{UE},k} \triangleq [x_{\text{UE},k}, y_{\text{UE},k}, z_{\text{UE},k}]^{\top}$, $\alpha_{\text{UE},k}$, and $v_{\text{UE},k}$ are respectively the UE's three-dimensional (3D) location, heading, and longitudinal speed. We represent the landmark types as $m \in \mathcal{M} \triangleq \{\text{RIS}, \text{RP}, \text{SP}\}$ and their respective locations by $\mathbf{x}_{\text{RIS}} = [x_{\text{RIS}}, y_{\text{RIS}}, z_{\text{RIS}}]^{\top}$, $\mathbf{x}_{\text{RP}} = [x_{\text{RP}}, y_{\text{RP}}, z_{\text{RP}}]^{\top}$, and $\mathbf{x}_{\text{SP}} = [x_{\text{SP}}, y_{\text{SP}}, z_{\text{SP}}]^{\top}$.

In the global coordinate system, the geometric center of antennas at the UE is located at $\mathbf{x}_{\text{UE},k}$ and the location of the n -th antenna element is denoted by $\mathbf{x}_{\text{UE},k}^n \triangleq [x_{\text{UE},k}^n, y_{\text{UE},k}^n, z_{\text{UE},k}^n]^{\top}$. In the local coordinate system, the UE antenna lies in the xz plane and the antenna element locations are denoted by $\check{\mathbf{X}}_{\text{UE},k} \triangleq [\check{\mathbf{x}}_{\text{UE},k}^1, \dots, \check{\mathbf{x}}_{\text{UE},k}^{N_{\text{UE}}}]$, where $\check{\mathbf{x}}_{\text{UE}}^n \triangleq [\check{x}_{\text{UE},k}^n, \check{y}_{\text{UE},k}^n, \check{z}_{\text{UE},k}^n]^{\top}$ is the location of the n -th antenna element. The relation between the 3D global and local locations of the UE antennas are expressed as $\check{\mathbf{x}}_{\text{UE},k}^n = \mathbf{O}_{\text{UE},k}^{\top} (\mathbf{x}_{\text{UE},k}^n - \mathbf{x}_{\text{UE},k})$, where $\mathbf{O}_{\text{UE},k}$ is the rotation matrix which rotates the local vector to the global one, and is defined as follows: $\mathbf{O}_{\text{UE},k} = [\mathbf{o}_{\text{UE},k,1}, \mathbf{o}_{\text{UE},k,2}, \mathbf{o}_{\text{UE},k,3}]$ with $\mathbf{o}_{\text{UE},k,1} = [\cos \alpha_{\text{UE},k}, \sin \alpha_{\text{UE},k}, 0]^{\top}$, $\mathbf{o}_{\text{UE},k,2} = [-\sin \alpha_{\text{UE},k}, \cos \alpha_{\text{UE},k}, 0]^{\top}$, and $\mathbf{o}_{\text{UE},k,3} = [0, 0, 1]^{\top}$, indicating the counter-clockwise rotation of the local UPA configuration around the z -axis. Similarly, we denote by $\mathbf{x}_{\text{RIS}} \triangleq [x_{\text{RIS}}, y_{\text{RIS}}, z_{\text{RIS}}]^{\top}$ the center of RIS in the global coordinate system, where $\check{\mathbf{x}}_{\text{RIS}}^n \triangleq [\check{x}_{\text{RIS}}^n, \check{y}_{\text{RIS}}^n, \check{z}_{\text{RIS}}^n]^{\top}$ is the location of its n -th reflective unit element, and the matrix $\check{\mathbf{X}}_{\text{RIS}} \triangleq [\check{\mathbf{x}}_{\text{RIS}}^1, \dots, \check{\mathbf{x}}_{\text{RIS}}^n]$ collects the locations of all RIS elements. Finally, \mathbf{O}_{RIS} represents the rotation matrix at the RIS, and we define $\check{\mathbf{x}}_{\text{RIS}}^n$ as $\check{\mathbf{x}}_{\text{RIS}}^n \triangleq \mathbf{O}_{\text{RIS}}^{\top} (\mathbf{x}_{\text{RIS}}^n - \mathbf{x}_{\text{RIS}})$.

Based on the latter definitions, the channel parameters (i.e., channel gains, Doppler shifts, ToAs, AoAs, and AoD) are obtained by the geometry relations corresponding to the above three types of paths (RIS, RP, and SP), as detailed in Appendix A.

C. Measurements' Modeling

The signal for each path in the received signal model (1) comes from the landmark (\mathbf{x}, m) . The number of landmarks as well as each landmark's location and type are unknown, and thus, we model the landmarks by an RFS $\mathcal{X} \triangleq \{(\mathbf{x}^1, m^1), \dots, (\mathbf{x}^I, m^I)\}$, where I denotes the random number of landmarks, having the set probability density function (PDF) $f(\mathcal{X})$ [49].

Based on the received signals $y_{t,k,s}$'s for different t and s , the UE separates the RIS path ($l = 0$) from the uncontrolled multipath ($l \neq 0$) (see the following Section III). To this end, we consider that a channel parameter estimation technique³ is adopted operating with $J_k + 1$ measurements (one measurement for $l = 0$ and a set of J_k ones for $l \neq 0$). Note that J_k is not necessarily equal to L , due to missed detections, false alarm, or clutter. The clutter is modeled as random channel parameters within the field-of-view (FoV) of the UE in its signal propagation environment, where the number of clutter measurements follows the Poisson distribution with intensity $c(\mathbf{z})$. Missed detections occur with adaptive detection probability $p_{D,k}(\mathbf{s}_k, \mathbf{x}, m) \in [0, 1]$ [52], when the landmark is within the FoV. In particular, the measurement for $l = 0$ is modeled as follows:

$$\mathbf{z}_k^0 = [\boldsymbol{\phi}_k^\top, \tau_{0,k}, v_{0,k}, \boldsymbol{\theta}_{0,k}^\top]^\top + \mathbf{r}_k^0, \quad (5)$$

with $\mathbf{r}_k^0 \sim \mathcal{N}(\mathbf{0}, \mathbf{R}_k^0)$ being the measurement noise, whereas the measurement for $l \neq 0$ is indexed by j and modeled as:

$$\mathbf{z}_k^j = \mathbf{h}(\mathbf{s}_k, \mathbf{x}, m) + \mathbf{r}_k^j, \quad (6)$$

where $\mathbf{h}(\mathbf{s}_k, \mathbf{x}, m) \triangleq [\tau_{l,k}, v_{l,k}, \boldsymbol{\theta}_{l,k}^\top]^\top$ with $\mathbf{r}_k^j \sim \mathcal{N}(\mathbf{0}, \mathbf{R}_k^j)$ being the measurement noise. Here, $\mathbf{R}_k^0 \in \mathbb{R}^{6 \times 6}$ and $\mathbf{R}_k^j \in \mathbb{R}^{4 \times 4}$ are the measurement noise covariance matrices, which are different for each path and depend on the precoder $\mathbf{f}_{t,k}$, combiner $\mathbf{w}_{t,k}$, and the RIS phase profile $\boldsymbol{\omega}_{t,k}$. Putting all above together, we represent the measurements as an RFS $\mathcal{Z}_k \triangleq \{\mathbf{z}_k^0, \dots, \mathbf{z}_k^{J_k}\}$. It is important to stress here that the associations between the L landmarks and the J_k NRIS signal paths is considered unknown in this paper.

³The channel parameters are assumed to be obtained by relevant channel estimation methods, such as the MD-ESPRIT [50], [51] or maximum likelihood [25] that perform close to the Cramér-Rao bound (CRB).

Sec. III-B], [28], and the spatial RIS phase profile for which capitalizes on the availability of the UE state information [30, Sec. III-C]. We then describe the proposed adaptive RIS phase profile design that enables the generation of multiple uniformly-spaced beams.

A. Overview of RIS Phase Profiles

1) *Time-Domain Design*: In order to separate the RIS-induced path from the other ones, the RIS phase profile is designed to be balanced in the time domain. For removing all NRIS paths with $l \neq 0$ in (1) (i.e., the UE-SPs-UE and UE-RPs-UE paths), we adopt the codebook design of [30, Sec. III-B]: $\tilde{\omega}_{\tilde{t},k} \in \mathbb{C}^{N_{\text{RIS}}}$ for $\tilde{t} = 1, \dots, T/2$, and $\omega_{2\tilde{t}-1,k} = \tilde{\omega}_{\tilde{t},k}$, $\omega_{2\tilde{t},k} = -\tilde{\omega}_{\tilde{t},k}$. In addition, we set the UE beamformers as $\mathbf{w}_{2\tilde{t}-1,k} = \mathbf{w}_{2\tilde{t},k} = \tilde{\mathbf{w}}_{\tilde{t},k}$ and $\mathbf{f}_{2\tilde{t}-1,k} = \mathbf{f}_{2\tilde{t},k} = \tilde{\mathbf{f}}_{\tilde{t},k}$. Following the latter definitions, we can remove the NRIS paths via computing $\tilde{y}_{\tilde{t},k,s}^{\text{RIS}} = 0.5(y_{2\tilde{t}-1,k,s} - y_{2\tilde{t},k,s})$, which yields the expression:

$$\begin{aligned} \tilde{y}_{\tilde{t},k,s}^{\text{RIS}} = & \frac{\sqrt{E_s}}{2} \tilde{\mathbf{w}}_{\tilde{t},k}^{\text{H}} \left(\sum_{l=1}^L \beta_{l,k} e^{j2\pi f_{l,k}^{\text{D}} T_0 (2\tilde{t}-1)} \mathbf{a}_{\text{UE}}(\boldsymbol{\theta}_{l,k}) \mathbf{a}_{\text{UE}}^{\text{T}}(\boldsymbol{\theta}_{l,k}) e^{-j2\pi \tau_{l,k} (s-1) \Delta_f} (1 - e^{j2\pi f_{l,k}^{\text{D}} T_0}) \right) \\ & + \beta_{0,k} e^{j2\pi f_{0,k}^{\text{D}} T_0 (2\tilde{t}-1)} \mathbf{a}_{\text{UE}}(\boldsymbol{\theta}_{0,k}) \tilde{\omega}_{\tilde{t},k}^{\text{T}} \mathbf{b}(\phi_k) \mathbf{a}_{\text{UE}}^{\text{T}}(\boldsymbol{\theta}_{0,k}) e^{-j2\pi \tau_{0,k} (s-1) \Delta_f} (1 + e^{j2\pi f_{0,k}^{\text{D}} T_0}) \tilde{\mathbf{f}}_{\tilde{t},k} + \tilde{n}_{\tilde{t},k,s}, \end{aligned} \quad (7)$$

where $\tilde{n}_{\tilde{t}} \sim \mathcal{CN}(0, \sigma_{\text{N}}^2/2)$ is the AWGN. Similar to the approximation of [25, Sec. IV-B], using the fact that $|f_{0,k}^{\text{D}} T_0| \ll 1$ is a negligible small value⁴ for the OFDM symbol duration, it holds for the residual terms caused by mobility that: $1 - e^{j2\pi f_{l,k}^{\text{D}} T_0} \approx 0$ and $1 + e^{j2\pi f_{0,k}^{\text{D}} T_0} \approx 2$. Therefore, expression (7) can be simplified as follows:

$$\tilde{y}_{\tilde{t},k,s}^{\text{RIS}} = \sqrt{E_s} \beta_{0,k} e^{j2\pi f_{0,k}^{\text{D}} T_0 (2\tilde{t}-1)} e^{-j2\pi \tau_{0,k} (s-1) \Delta_f} \tilde{\mathbf{w}}_{\tilde{t},k}^{\text{H}} \mathbf{a}_{\text{UE}}(\boldsymbol{\theta}_{0,k}) \tilde{\omega}_{\tilde{t},k}^{\text{T}} \mathbf{b}(\phi_k) \mathbf{a}_{\text{UE}}^{\text{T}}(\boldsymbol{\theta}_{0,k}) \tilde{\mathbf{f}}_{\tilde{t},k} + \tilde{n}_{\tilde{t},k,s}, \quad (8)$$

which implies that the RIS-reflected path can be processed separately. Similarly, we can obtain the NRIS paths using the simple mathematical operation: $\tilde{y}_{\tilde{t},k,s}^{\text{NRIS}} \approx 0.5(y_{2\tilde{t}-1,k,s} + y_{2\tilde{t},k,s})$.

2) *Spatial-Domain Design*: The conventional spatial designs are the random or directional RIS phase profiles, which are described in the following.

- *Random Profile*: When the prior PDF of the UE location at each time step k , $f(\mathbf{x}_{\text{UE},k})$, is uninformative or does not exist, random RIS phase profiles are commonly used, i.e., $\tilde{\omega}_{\tilde{t},k}^n = e^{j\phi_{\tilde{t},k}^n}$, where $\tilde{\omega}_{\tilde{t},k}^n$ denotes $\tilde{\omega}_{\tilde{t},k}$'s n -th element and $\phi_{\tilde{t},k}^n \sim [0, 2\pi)$ is the RIS phase which is assumed independent and identically distributed for n and \tilde{t} [25], [28], [37], [53].

⁴In the considered mmWave setups with parameters as described in Table I, the value for $f_{0,k}^{\text{D}} T_0$ is about 1.5×10^{-11} .

- *Directional Profile*: When an informative prior $f(\mathbf{x}_{\text{UE},k})$ is available, we may use directional RIS phase profiles $\tilde{\omega}_{\tilde{t},k}$ [25], [26], [53]. From $f(\mathbf{x}_{\text{UE},k})$, one can generate $T/2$ azimuth and elevation samples as $\{\phi_{\tilde{t},k}\}_{\tilde{t}=1}^{T/2}$ with $\phi_{\tilde{t},k} \triangleq [\phi_{\tilde{t},k}^{\text{az}}, \phi_{\tilde{t},k}^{\text{el}}]^\top$. Then, using (3), we yields:

$$\tilde{\omega}_{\tilde{t},k} = \exp(-2j(\check{\mathbf{X}}_{\text{RIS}})^\top \mathbf{g}(\phi_{\tilde{t},k})), \quad (9)$$

which leads to so-called fine pencil beams [54].

The main drawback with the RIS directional phase profiles is that, when the RIS is large, each reflective beam is narrow, indicating that the $T/2$ RIS phase profiles may not adequately cover the angular uncertainty region determined by the prior $f(\mathbf{x}_{\text{UE},k})$. In that case, there is a risk that the UE location is missed by the finite number of directional beams.

B. Proposed Adaptive RIS Phase Profiles

In order to generate spatially-uniform beams, we herein design the RIS phase profile $\tilde{\omega}_{\tilde{t},k}$ for $\tilde{t} = 1, \dots, T/2$. Using the given UE position prior $f(\mathbf{x}_{\text{UE},k})$, we select the boundary of its angular uncertainty with the goal to uniformly illuminate it with some probability $P_E \in [0, 1)$.

a) Definition of the ‘Angular Uncertainty Region: Our objective is to first determine the angular uncertainty in the azimuth and elevation angles, denoted respectively by $[\phi_{\min,k}^{\text{az}}, \phi_{\max,k}^{\text{az}}]$ and $[\phi_{\min,k}^{\text{el}}, \phi_{\max,k}^{\text{el}}]$. We adopt the assumption that the density of the UE position $\mathbf{x}_{\text{UE},k}$ is Gaussian distributed, hence, the predicted UE position PDF is represented as $f(\mathbf{x}_{\text{UE},k} | \mathcal{Z}_{1:k-1}) = \mathcal{N}(\mathbf{x}_{\text{UE},k|k-1}, \mathbf{P}_{\text{UE},k|k-1})$, where $\mathbf{x}_{\text{UE},k|k-1}$ and $\mathbf{P}_{\text{UE},k|k-1}$ are the mean and covariance, which can be extracted from the predicted density in the Bayesian recursion. Then, the position samples are drawn as $\mathbf{x}_{\text{UE},k}^p \sim \mathcal{N}(\mathbf{x}_{\text{UE},k|k-1}, \mathbf{P}_{\text{UE},k|k-1})$ and N_{pos} samples within the confidence region with a particular probability P_E are selected. For the considered multivariate Gaussian distribution, the condition for satisfying the confidence region is [55]: $(\boldsymbol{\mu}^p)^\top \mathbf{P}_{\text{UE},k|k-1}^{-1} \boldsymbol{\mu}^p \leq T_E$, where $\boldsymbol{\mu}^p \triangleq \mathbf{x}_{\text{UE},k|k-1} - \mathbf{x}_{\text{UE},k}^p$ and T_E is a threshold computed as $T_E = Q_{\chi_{D_F}^2}(P_E)$, with $Q_{\chi_{D_F}^2}(P_E)$ being the chi-square-distributed quantile function for P_E with D_F degrees of freedom for $\mathbf{x}_{\text{UE},k}$. Using the latter considerations, we design the angular uncertainty ranges as follows:

$$\phi_{\min,k}^{\text{az}} = \min_p \text{atan2}(\check{y}_{\text{UR},k}^p, \check{x}_{\text{UR},k}^p), \quad \phi_{\max,k}^{\text{az}} = \max_p \text{atan2}(\check{y}_{\text{UR},k}^p, \check{x}_{\text{UR},k}^p), \quad (10)$$

$$\phi_{\min,k}^{\text{el}} = \min_p \text{acos}(\check{z}_{\text{UR},k}^p / d_{\text{UR},k}^p), \quad \phi_{\max,k}^{\text{el}} = \max_p \text{acos}(\check{z}_{\text{UR},k}^p / d_{\text{UR},k}^p), \quad (11)$$

where $\check{\mathbf{x}}_{\text{UR},k}^p \triangleq [\check{x}_{\text{UR},k}^p, \check{y}_{\text{UR},k}^p, 0]^\top$ and $d_{\text{UR},k}^p = \|\check{\mathbf{x}}_{\text{UR},k}^p\|$, which can be obtained via the geometric relations in Appendix A. In addition, $\check{\mathbf{x}}_{\text{UR},k}^p = \mathbf{O}_{\text{RIS}}^\top \mathbf{x}_{\text{UR},k}^p$ with $\mathbf{x}_{\text{UR},k}^p = \mathbf{x}_{\text{UE},k}^p - \mathbf{x}_{\text{RIS}}$. In order

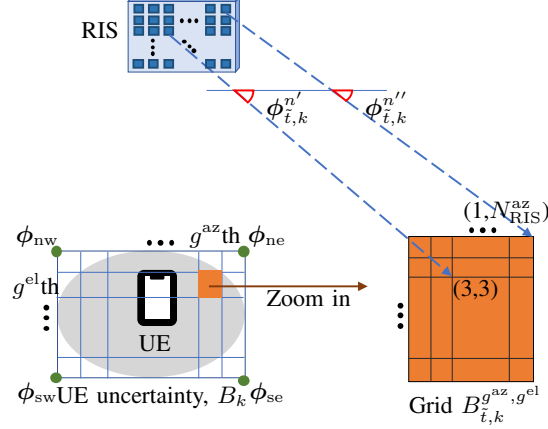


Fig. 3: An example illustration of the RIS phase profiles for multiple spatially-uniform beams. The UE uncertainty is represented by a rectangle B_k , which is divided into $T/2$ grids, inspired by our proposed time-domain RIS profile design. This indicates that two consecutive transmissions suffice to cover the whole grid. During each transmission, each RIS element's phase is configured to direct the induced reflection in a slightly different direction than any other one, in order for all to cover all points of the grid. For example, the distinct elements n' and n'' steer at the angles $\phi_{i,k}^{n'}$ and $\phi_{i,k}^{n''}$ with $\phi_{i,k}^{n'} \neq \phi_{i,k}^{n''}$.

to represent the latter angular uncertainty ranges in the azimuth and elevation domains, we generate a rectangle (grid) with the four points $\phi_{sw} \triangleq [\phi_{\min,k}^{az}, \phi_{\min,k}^{el}]^\top$, $\phi_{se} \triangleq [\phi_{\max,k}^{az}, \phi_{\min,k}^{el}]^\top$, $\phi_{nw} \triangleq [\phi_{\min,k}^{az}, \phi_{\max,k}^{el}]^\top$, $\phi_{ne} \triangleq [\phi_{\max,k}^{az}, \phi_{\max,k}^{el}]^\top$, which is from now on represented by B_k .

b) Uniform Coverage of the Uncertainty Region: We now devise the RIS phase profiles $\tilde{\omega}_{i,k} \triangleq [\tilde{\omega}_{i,k}^1, \dots, \tilde{\omega}_{i,k}^{N_{RIS}}]^\top$ in (9) by designing $\phi_{i,k} \triangleq [(\phi_{i,k}^1)^\top, \dots, (\phi_{i,k}^{N_{RIS}})^\top]^\top$, as illustrated in Fig. 3. We first note that, due to the half of transmission diversity offered by the time-domain RIS profiles, two consecutive pilot transmissions suffice to cover the angular uncertainty of the grid during each time interval k . We thus divide the rectangle B_k into T^{az} horizontal and T^{el} vertical slices such that $T^{az} \times T^{el} = T/2$, where each \tilde{t} -th box, with $\tilde{t} = 1, \dots, T/2$, lies in between the g^{az} -th column and g^{el} -th row of the grid B_k . This defined the box $B_{i,k}^{g^{az}, g^{el}}$ with $g^{az} = \tilde{t} - T^{az}(\text{ceil}(\tilde{t}/T^{az}) - 1)$ and $g^{el} = \text{ceil}(\tilde{t}/T^{az})$, where $\text{ceil}(x)$ returns the smallest integer that is greater or equal to x . To illuminate all grid points $B_{i,k}^{g^{az}, g^{el}}$ in each transmission \tilde{t} , each RIS element's phase is configured to a slightly different direction to point at a points of the grid. The phase configuration of each n -th RIS element is thus designed as $\phi_{i,k}^n = [\phi_{\min,k}^{az} + \zeta_k^{az}(g^{az} - 1)/T^{az} + \zeta_k^{az}(n^{az} - 1)/(T^{az}(N_{RIS}^{az} - 1)), \phi_{\min,k}^{el} + \zeta_k^{el}(g^{el} - 1)/T^{az} + \zeta_k^{el}(n^{el} - 1)/(T^{az}(N_{RIS}^{el} - 1))]^\top$, where $\zeta_k^{az} = \phi_{\max,k}^{az} - \phi_{\min,k}^{az}$, $\zeta_k^{el} = \phi_{\max,k}^{el} - \phi_{\min,k}^{el}$, $n^{az} = n - N_{az}^{az}(\text{ceil}(\tilde{n}/N_{RIS}^{az}) - 1)$, and $n^{el} = \text{ceil}(\tilde{n}/N_{RIS}^{az})$. By selecting the intersection points of evenly separated N_{RIS}^{az} vertical and N_{RIS}^{el} horizontal line segments on the grid, we can generate $N_{RIS} = N_{RIS}^{az} \times N_{RIS}^{el}$ points at the

grid. Finally, we design the phase profile for each n -th RIS element as follows:

$$\tilde{\omega}_{t,k}^n = \exp(-2j(\tilde{\mathbf{x}}_{\text{RIS}}^n)^\top \mathbf{g}(\phi_{t,k}^n)). \quad (12)$$

Remark 1 (Interpretation of (12)). *Conceptually, the phase of each n -th RIS element is configured with respect to the RIS phase center to direct a beam in a slightly different direction than this. Hence, $\phi_{t,k}^n \neq \phi_{t,k}^{n'}$ when $n \neq n'$, unless the uncertainty region is a single point, in which case (12) reverts to a conventional pencil beam as in (9).*

IV. PROPOSED RIS-AIDED SLAM ESTIMATION

In this section, we propose an extension of the MPMB-SLAM filter⁵ [3], with the intention to account for the fact that the RIS-induced path can be separated using the time-domain RIS phase profiles, as presented in the previous Section III-A1.

A. Preliminaries

We introduce the notation I_{k-1} to denote the number of detected landmarks, with each of them indexed by i . $f(\mathbf{s}_k | \mathcal{Z}_{1:k-1}) \triangleq f_{p,k}(\mathbf{s}_k)$ and $f(\mathbf{s}_k | \mathcal{Z}_{1:k}) \triangleq f_{u,k}(\mathbf{s}_k)$ represent the prior and updated PDFs of the UE state. Undetected landmarks that have been never detected are modeled by a Poisson point process (PPP), which can be characterized by its intensity. To this end, $\lambda(\mathbf{x}, m | \mathcal{Z}_{1:k-1}) \triangleq \lambda_{p,k}(\mathbf{x}, m)$ and $\lambda(\mathbf{x}, m | \mathcal{Z}_{1:k}) \triangleq \lambda_{u,k}(\mathbf{x}, m)$ are respectively the predicted and updated intensities for undetected landmarks of type m . Detected landmarks that have been previously detected at least once follow a multi-Bernoulli (MB) process, and each landmark is characterized by a Bernoulli density. $f^i(\mathbf{x}, m | \mathcal{Z}_{1:k-1}) \triangleq f_{p,k}^i(\mathbf{x}, m)$ ($f^i(\mathbf{x}, m | \mathcal{Z}_{1:k}) \triangleq f_{u,k}^i(\mathbf{x}, m)$) and $r_{p,k}^i$ ($r_{u,k}^i$) represent the predicted (updated) density of detected landmark i of type m and its existence probability, respectively. $g(\mathbf{z}_k^0 | \mathbf{s}_k)$ and $g(\mathbf{z}_k^j | \mathbf{s}_k, \mathbf{x}, m)$ denote the measurement likelihood functions of (5) and (6), respectively.

B. Update Step

At each discrete time k , the following prior components are given: the intensities of the undetected landmarks $\{\lambda_{p,k}(\mathbf{x}, m)\}_{m \in \{\text{RP}, \text{SP}\}}$, the predicted UE state density $f_{p,k}(\mathbf{s}_k)$, the RIS state density $f^1(\mathbf{x}, \text{RIS})$, the RIS existence probability r^1 , as well as the densities and existence probabilities of the detected landmarks $\{\{f_{p,k}^i(\mathbf{x}, m)\}_{m \in \{\text{RP}, \text{SP}\}}, r_{p,k}^i\}_{i=2}^{I_{k-1}}$.

⁵The MPMB-SLAM filter is efficient with respect to the performance trade-off between complexity and accuracy for RFS-based sequential Bayesian estimation. Very recently, it has been applied for parameter estimation in mmWave vehicular systems [3].

1) *Statistics and Map Updates:* Due to the distinguishable RIS path, there is no update for the RIS Bernoulli components $f^1(\mathbf{x}_{\text{RIS}})$ and r^1 , whereas the Poisson multi-Bernoulli (PMB) components of the other landmarks are updated with the measurements $\tilde{\mathcal{Z}}_k = \mathcal{Z}_k \setminus \{\mathbf{z}_k^0\}$, where ‘\’ indicates the set difference. In the PMB density, a landmark set is divided into two independent subsets: a set of undetected landmarks (landmarks that exist but have not yet been detected); and a set of detected landmarks (landmarks that have been associated to at least one previous measurement). In the update step, each set goes through two cases: missed detections (when a landmark is not detected) and detections (when a landmark is detected by any measurement in $\tilde{\mathcal{Z}}_k$), leading to an exponentially increasing number of cases. We will next use the definitions $h_{\text{p},k}^{\text{U}}(\mathbf{s}_k, \mathbf{x}, m) \triangleq f_{\text{p},k}(\mathbf{s}_k)\lambda_{\text{p},k}(\mathbf{x}, m)$ and $h_{\text{p},k}^{\text{D},i}(\mathbf{s}_k, \mathbf{x}, m) \triangleq f_{\text{p},k}(\mathbf{s}_k)f_{\text{p},k}^i(\mathbf{x}, m)$.

- i) *Intensity of undetected landmarks that remained undetected:* The updated intensity corresponds to the missed detection $1 - \text{p}_{\text{D},k}(\mathbf{s}_k, \mathbf{x}, m)$ of undetected landmarks $\lambda_{\text{p},k}(\mathbf{x}, m)$, integrated over the UE state density $f_{\text{p},k}(\mathbf{s}_k)$. Mathematically, this is given by:

$$\lambda_{\text{u},k}(\mathbf{x}, m) = \int (1 - \text{p}_{\text{D},k}(\mathbf{s}_k, \mathbf{x}, m)) h_{\text{p},k}^{\text{U}}(\mathbf{s}_k, \mathbf{x}, m) \text{d}\mathbf{s}_k. \quad (13)$$

- ii) *Density of a new landmark that was detected for the first time with a measurement \mathbf{z}_k^j :* With $\mathbf{z}_k^j \in \tilde{\mathcal{Z}}_k$, new Bernoulli components are generated by the prior $h_{\text{p},k}^{\text{U}}(\mathbf{s}_k, \mathbf{x}, m)$ using the likelihood function $g(\mathbf{z}_k^j | \mathbf{s}_k, \mathbf{x}, m)$, which is being weighted by the detection probability $\text{p}_{\text{D},k}(\mathbf{s}_k, \mathbf{x}, m)$, yielding the density:

$$f_{\text{u},k}^j(\mathbf{x}, m) \propto \int \text{p}_{\text{D},k}(\mathbf{s}_k, \mathbf{x}, m) h_{\text{p},k}^{\text{U}}(\mathbf{s}_k, \mathbf{x}, m) g(\mathbf{z}_k^j | \mathbf{s}_k, \mathbf{x}, m) \text{d}\mathbf{s}_k, \quad (14)$$

where $\rho_k^j = \sum_m \iint \text{p}_{\text{D},k}(\mathbf{s}_k, \mathbf{x}, m) h_{\text{p},k}^{\text{U}}(\mathbf{s}_k, \mathbf{x}, m) g(\mathbf{z}_k^j | \mathbf{s}_k, \mathbf{x}, m) \text{d}\mathbf{s}_k \text{d}\mathbf{x}$ is the normalization constant. The updated existence probability is $r_{\text{u},k}^j = \rho_k^j / (\rho_k^j + c(\mathbf{z}_k^j))$, accounting for the probability that the hypothesized landmark was actually clutter.

- iii) *Density of a previously detected landmark that was miss-detected:* In this case, the prior $h_{\text{p},k}^{\text{D},i}(\mathbf{s}_k, \mathbf{x}, m)$ is multiplied by the missed detection probability $(1 - \text{p}_{\text{D},k}(\mathbf{s}_k, \mathbf{x}, m))$ to obtain the density:

$$f_{\text{u},k}^{0,i}(\mathbf{x}, m) \propto \int (1 - \text{p}_{\text{D},k}(\mathbf{s}_k, \mathbf{x}, m)) h_{\text{p},k}^{\text{D},i}(\mathbf{s}_k, \mathbf{x}, m) \text{d}\mathbf{s}_k, \quad (15)$$

where $\rho_k^{0,i} = \sum_m \iint (1 - \text{p}_{\text{D},k}(\mathbf{s}_k, \mathbf{x}, m)) h_{\text{p},k}^{\text{D},i}(\mathbf{s}_k, \mathbf{x}, m) \text{d}\mathbf{s}_k \text{d}\mathbf{x}$ is the normalization constant. The updated existence probability in this case is given by $r_{\text{u},k}^{0,i} = r_{\text{p},k}^i \rho_k^{0,i} / (1 - r_{\text{p},k}^i + r_{\text{p},k}^i \rho_k^{0,i})$.

- iv) *Density of a previously detected landmark that was detected again with a measurement \mathbf{z}_k^j :* With $\mathbf{z}_k^j \in \tilde{\mathcal{Z}}_k$, the Bernoulli components of landmark i , for $i = \{2, \dots, I_{k-1}\}$, are updated

by the product of the prior $h_{p,k}^{D,i}(\mathbf{s}_k, \mathbf{x}, m)$ times the likelihood $g(\mathbf{z}_k^j | \mathbf{s}_k, \mathbf{x}, m)$, while being corrected with the detection probability $p_{D,k}(\mathbf{s}_k, \mathbf{x}, m)$; the following expression is deduced:

$$f_{u,k}^{j,i}(\mathbf{x}, m) \propto \int p_{D,k}(\mathbf{s}_k, \mathbf{x}, m) h_{p,k}^{D,i}(\mathbf{s}_k, \mathbf{x}, m) g(\mathbf{z}_k^j | \mathbf{s}_k, \mathbf{x}, m) d\mathbf{s}_k, \quad (16)$$

where $\rho_k^{j,i} = \sum_m \iint p_{D,k}(\mathbf{s}_k, \mathbf{x}, m) h_{p,k}^{D,i}(\mathbf{s}_k, \mathbf{x}, m) g(\mathbf{z}_k^j | \mathbf{s}_k, \mathbf{x}, m) d\mathbf{s}_k d\mathbf{x}$ is the normalization constant. The updated existence probability is now $r_{u,k}^{j,i} = 1$.

In conclusion, the landmark update procedure consists of the four steps i)–iv), and the updated densities and likelihood functions can be computed by a non-linear Kalman filter [56]. We thus have $|\tilde{\mathcal{Z}}_k|$ new landmarks (step ii) and for each of the I_{k-1} previously detected landmarks, we have $|\tilde{\mathcal{Z}}_k| + 1$ possible Bernoulli densities (steps iii and iv). Since each non-RIS measurement⁶ can only be associated to at most one landmark, the so-called marginal association probabilities should be computed [57, Fig. 9] based on the normalization constants $\rho_k^{i,0}$ and $\rho_k^{i,j}$. From these, each previously detected landmark gives rise to a mixture density with weights given by the marginal association probabilities, and each new landmark's existence probability is reduced by the corresponding marginal association probability [57, Fig. 10].

2) *UE Update*: We compute the global association probabilities through the product of the normalization constants of valid track- and measurement-oriented associations. We calculate the most likely association using Murty's algorithm [58] (a generalization of the Hungarian algorithm for solving linear assignment problems). Then, with each previously detected landmark i , we have an associated measurement set, denoted by $\mathcal{Z}_k^{a_i}$, which may be empty or contain one element from $\tilde{\mathcal{Z}}_k$. Note that the RIS measurement \mathbf{z}_k^0 is utilized in the UE density update (as in [30]) and never generates a newly detected landmark. The update of the UE state density [3, Proposition 3] is thus simplified as follows:

$$f_{u,k}(\mathbf{s}_k) \propto f_{p,k}(\mathbf{s}_k) g(\mathbf{z}_k^0 | \mathbf{s}_k) \prod_{i=2}^{I_{k-1}} q_i(\mathcal{Z}_k^{a_i} | \mathbf{s}_k), \quad (17)$$

where $q_i(\mathcal{Z}_k^{a_i} | \mathbf{s}_k)$ for $i = 2, \dots, I_{k-1}$ is given by

$$q_i(\mathcal{Z}_k^{a_i} | \mathbf{s}_k) = \begin{cases} r_{p,k}^i \sum_m \int p_D(\mathbf{s}_k, \mathbf{x}, m) f_{p,k}^i(\mathbf{x}, m) g(\mathbf{z}_k^j | \mathbf{s}_k, \mathbf{x}, m) d\mathbf{x}, & \mathcal{Z}_k^{a_i} = \{\mathbf{z}_k^j\} \\ r_{p,k}^i \sum_m \int (1 - p_D(\mathbf{s}_k, \mathbf{x}, m)) f_{p,k}^i(\mathbf{x}, m) d\mathbf{x} + 1 - r_{p,k}^i, & \mathcal{Z}_k^{a_i} = \emptyset \end{cases}. \quad (18)$$

⁶Due to the distinguishable RIS path, the associations corresponding to landmark $i = 1$ and measurement \mathbf{z}^0 are known.

C. Prediction Step

1) *Landmark*: Since the undetected landmarks are fixed, the intensity for $m = \{\text{RP}, \text{SP}\}$ is predicted as $\lambda_{p,k+1}(\mathbf{x}_{k+1}, m) = \int P_S \lambda_{u,k}(\mathbf{x}_k, m) d\mathbf{x} + \lambda_{B,k+1}(\mathbf{x}_{k+1}, m)$, where P_S is the survival probability and $\lambda_{B,k+1}(\mathbf{x}_{k+1}, m)$ is the birth intensity. The Bernoulli position density for the RP depends on UE's heading and speed. For RP prediction, we introduce the notation $\tilde{\mathbf{s}}_k \triangleq [\alpha_{\text{UE},k}, v_{\text{UE},k}]^\top$ with $f_{u,k}(\tilde{\mathbf{s}}_k)$ extracted from $f_{u,k}(\mathbf{s}_k)$ in (17), and $f(\mathbf{x}_{k+1}, \tilde{\mathbf{s}}_{k+1} | \mathbf{x}_k, \tilde{\mathbf{s}}_k)$ being the known transition density. Then, the predicted density is obtained as $f_{p,k+1}^i(\mathbf{x}, \text{RP}) = \int f(\mathbf{x}_{k+1}, \tilde{\mathbf{s}}_{k+1} | \mathbf{x}_k, \tilde{\mathbf{s}}_k) f_{u,k}(\tilde{\mathbf{s}}_k) P_S f_{u,k}^i(\mathbf{x}_k, \text{RP}) d\mathbf{x}_k d\tilde{\mathbf{s}}_k d\tilde{\mathbf{s}}_{k+1}$. For the fixed SP, the Bernoulli components are predicted as $f_{p,k+1}^i(\mathbf{x}_{k+1}, \text{SP}) = f_{u,k}^i(\mathbf{x}, \text{SP})$ and $r_{p,k+1}^i = P_S r_{u,k}^i$.

2) *UE*: The UE density is finally predicted as $f_{p,k+1}(\mathbf{s}_{k+1}) = \int f(\mathbf{s}_{k+1} | \mathbf{s}_k) f_{u,k}(\mathbf{s}_k) d\mathbf{s}_k$, in which $f(\mathbf{s}_{k+1} | \mathbf{s}_k)$ is the known transition density of the dynamic model for the UE state. We finally extract the prior density of the UE position $f_{p,k+1}(\mathbf{x}_{\text{UE},k+1})$, using $f_{p,k+1}(\mathbf{s}_{k+1})$, which is utilized for the RIS phase profiles of Section III at each next time instant $k + 1$.

V. NUMERICAL RESULTS AND DISCUSSION

In this section, we present simulation results demonstrating the efficiency of the proposed SLAM method in conjunction with the new RIS phase profiles. We first detail the simulation setup and then investigate the performance of the proposed RIS-enabled SLAM scheme over various operation parameters.

A. Simulation Setup

The simulation parameters used in our performance evaluations are summarized in Table I. The size of the propagation environment was set to $[40, 100] \text{ m} \times [-30, 70] \text{ m} \times [0, 40] \text{ m}$, and the size of the road, where the UE moves, was $[40, 60] \text{ m} \times [-20, 60] \text{ m}$ with $z = 0$. In the propagation environment, we have considered a single RIS, a single LS, four SPs, and a single UE. During $K = 20$ time intervals, the UE dynamics followed the constant turn model [48] with polar velocity and known turn rate. Hence, the UE state evolution was given by $\mathbf{s}_{\text{UE},k+1} = \mathbf{m}(\mathbf{s}_{\text{UE},k}) + \mathbf{q}_k$, where $\mathbf{m}(\cdot)$ is the transition function and $\mathbf{q}_k \sim (\mathbf{0}, \mathbf{Q}_k)$ is the process noise. The function $\mathbf{m}(\cdot)$, considering the known constant turn rate $\rho_{\text{UE},k}$, can be derived as [48]: $\mathbf{m}(\mathbf{s}_{\text{UE},k+1}) = \mathbf{s}_{\text{UE},k} + [\Delta_{x,\text{UE}}, \Delta_{y,\text{UE}}, 0, \rho_{\text{UE},k} \Delta, v_{\text{UE},k}]^\top$, where $\Delta_{x,\text{UE}} = \frac{v_{\text{UE},k}}{\rho_{\text{UE},k}} (\sin(\alpha_{\text{UE},k} + \rho_{\text{UE},k} \Delta) - \sin \alpha_{\text{UE},k})$ and $\Delta_{y,\text{UE}} = \frac{v_{\text{UE},k}}{\rho_{\text{UE},k}} (-\cos(\alpha_{\text{UE},k} + \rho_{\text{UE},k} \Delta) + \cos \alpha_{\text{UE},k})$, and $\mathbf{Q}_k = \text{diag}(\sigma_x^2, \sigma_y^2, \sigma_z^2, \sigma_\alpha^2, \sigma_v^2)$ with $\sigma_x = 0.2 \text{ m}$, $\sigma_y = 0.2 \text{ m}$, $\sigma_z = 0 \text{ m}$, $\sigma_\alpha = 10^{-3} \text{ rad}$, and $\sigma_v^2 = 0.2 \text{ m/s}$; we have set $\Delta = 0.5 \text{ s}$

TABLE I: The Simulation Parameters Used in the Performance Evaluations.

Parameter	Value	Parameter	Value
RIS array size	$N_{\text{RIS}} = 2500 (50 \times 50)$	UE array size	$N_{\text{UE}} = 16 (4 \times 4)$
Number of transmissions	$T = 20$	Carrier frequency	$f_c = 30 \text{ GHz}$
Speed of light	$c = 3 \times 10^8 \text{ m/s}$	Wavelength	$\lambda = 1 \text{ cm}$
Bandwidth	$B = 200 \text{ MHz}$	Subcarrier spacing	$\Delta_f = 120 \text{ kHz}$
Number of subcarriers	$N_{\text{SC}} = 1600$	CP overhead	$\epsilon_{\text{CP}} = 0.07$
Number of CP subcarriers	$N_{\text{CP}} = 112$	Transmission power	$E_s N_{\text{SC}} \Delta_f = 20 \text{ dBm}$
Symbol duration	$T_S = 8 \mu\text{s}$	CP duration	$T_{\text{CP}} = 0.56 \mu\text{s}$
Signal duration	$T_o = T_S + T_{\text{CP}} = 8.07 \mu\text{s}$	Noise PSD	$N_0 = -174 \text{ dBm/Hz}$
Noise figure	$N_{\text{NF}} = 8 \text{ dB}$	Signal noise variance	$\sigma_N^2 = N_0 N_{\text{NF}} = -166 \text{ dBm/Hz}$
RIS 3D position	$\mathbf{x}_{\text{RIS}} = [40, 0, 20]^T \text{ m}$	LS plane's point	$x = 100 \text{ m}$

and $\rho_{\text{UE},k} = 2 \times 10^{-6} \text{ rad/s}$. The RIS lied on a vertical wall on the yz plane, the UE movement was parallel to the LS, and one RP was visible from the LS at every time instant k . Thus, K RPs were detected and the RP locations were set to $\mathbf{x}_{\text{RP},k} = [100, y_{\text{UE},k}, 0] \text{ m}$ for $k = 1, \dots, 20$. The SPs locations were set to $\mathbf{s}_{\text{SP}}^1 = [40, -20, z_{\text{SP}}]^T \text{ m}$, $\mathbf{s}_{\text{SP}}^2 = [60, 5, z_{\text{SP}}]^T \text{ m}$, $\mathbf{s}_{\text{SP}}^3 = [40, 30, z_{\text{SP}}]^T \text{ m}$, and $\mathbf{s}_{\text{SP}}^4 = [60, 55, z_{\text{SP}}]^T \text{ m}$ with $z_{\text{SP}} \sim \mathcal{U}(0, 10)$. The RIS and RPs were always visible, while SPs were only visible when the SPs exist within a FoV distance of $r_{\text{FOV}} = 50 \text{ m}$ from the⁷ UE. Within the FoV, we set the detection probability as $P_{\text{D}} = 0.95$, RPs and SPs were detected with P_{D} , and the RIS was always detected. The clutter intensity was set to $c(\mathbf{z}) = 2.1 \times 10^{-6}$, the number of clutter was Poisson distributed with mean $\mu_{\text{Poi}} = 1$, and the measurement for clutter \mathbf{z}_k was randomly generated within the propagation environment. The probability for the confidence region P_{E} was set to 0.99 with $D_{\text{F}} = 2$ degrees of freedom, yielding $T_{\text{E}} = -2 \log P_{\text{E}}$.

We adopted the complex path gain model $\beta_{l,k} = |\beta_{l,k}| e^{-j(2\pi f_c \tau_{l,k} + \nu_{\text{G}})}$ for $l = 0, \dots, L$, where the amplitudes $|\beta_{l,k}|$ for specular reflection, scatter one [59, eq. (45)], and for RIS reflection [60, eq. (22)] were set as: $|\beta_{l,k}| = \frac{\lambda}{4\pi} \frac{\lambda \cos(\varphi_0)^{2q_0}}{16d_{\text{UR},k}^2}$ for the RIS; $|\beta_{l,k}| = \frac{\lambda}{4\pi} \frac{\sqrt{\Gamma_{\text{R}}}}{2d_{\text{IU},k}^{(\text{RP})}}$ for the RP; and $|\beta_{l,k}| = \frac{\lambda}{4\pi} \frac{\sqrt{S_{\text{RCS}}}}{\sqrt{4\pi}(d_{\text{IU},k}^{(\text{SP})})^2}$ for the SP. We have considered $\nu_{\text{G}} \sim \mathcal{U}[0, 2\pi)$ being the unknown phase offset, $q_0 = 0.285$, $\cos(\varphi_0) = (\mathbf{x}_{\text{UR}}^{\text{T}} \mathbf{n}_{\text{RIS}} / d_{\text{UR},k})$, $\mathbf{n}_{\text{RIS}} = [1, 0, 0]^T$ (normal vector of the plane where the RIS elements lie), $\Gamma_{\text{R}} = 0.7$ was the reflection coefficient, and $S_{\text{RCS}} = 50 \text{ m}^2$ was the square of the radar cross section.

To implement the MPMB-SLAM filter, we adopted the parameters of [3, Sec. VI.A]. Specifically, in steps i) and ii) of Section IV-B, we set $p(\mathbf{s}_k, \mathbf{x}, m) = 0.95$, and in steps iii) and

⁷The NRIS paths were only visible if their SNRs were sufficiently high.

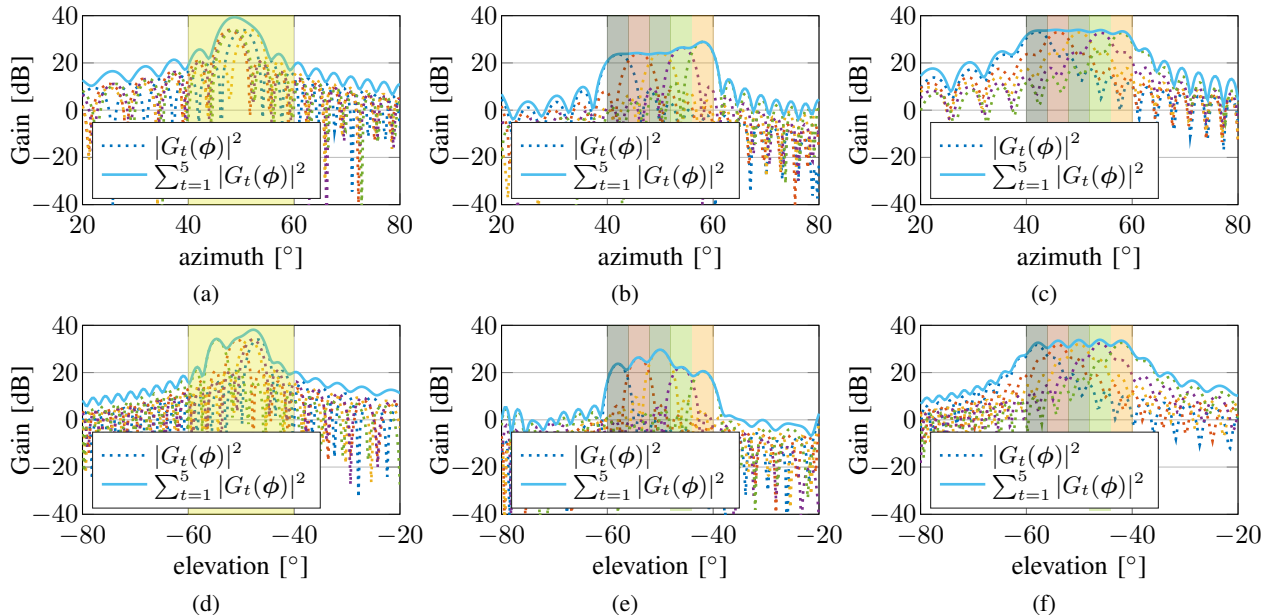


Fig. 4: Beampatterns of the 2D RIS in the azimuth domain ((a)–(c)) with the fixed elevation $\phi_0^{\text{el}} = -50^\circ$, and in the elevation domain ((e)–(f)) with the fixed azimuth $\phi_0^{\text{az}} = 50^\circ$, aiming the highlighted UE angular uncertainty region spanning onto $[40^\circ, 60^\circ]$ in the azimuth and $[-60^\circ, 40^\circ]$ in the elevation. The beampatterns in (a) and (d) were generated with directional phases; (b) and (e) with the optimized phase approach in [39]; and in (c) and (f) via the proposed uniform phase in Section III-B.

iv), we set $p(\mathbf{s}_k, \mathbf{x}, m) = 0.95$ if $M_d < T_G$, otherwise, $p(\mathbf{s}_k, \mathbf{x}, m) \approx 0$, where M_d is the ellipsoidal gating distance with gate probability $P_G = 0.99$. We have set the survival probability as $P_S = 0.99$, and the approximated Gaussian densities were computed via the cubature Kalman filter approximation [1], [3], [61] with the measurement noise covariance $\mathbf{R}_{U,k}^j = 4 \times \mathbf{R}_k^j$ for numerical robustness. The weight thresholds for pruning a Bernoulli, Gaussian of the intensity, and global hypothesis were respectively 10^{-5} , 5×10^{-10} , and 10^{-4} . The landmark i was detected if $r_{u,k}^i > T_{\text{EP}} = 0.4$, and its landmark type and position were respectively estimated as $\hat{m} = \max_m \rho_k^i(m)$ and $\hat{\mathbf{x}} = \int \mathbf{x} f_{u,k}^i(\mathbf{x}, \hat{m}) d\mathbf{x}$. The performance results that follows were obtained by averaging over 500 Monte Carlo simulation runs. To evaluate the performance of localization and radio mapping, the mean absolute error (MAE) and the generalized optimal subpattern assignment (GOSPA) distance [62] metrics were utilized.

B. Positioning Performance

As benchmark reflective beampatterns, we have used the following RIS phase profiles: *i*) random phases, where the individual element phases were drawn randomly from $[0, 2\pi]$ (see, Section III-A2); and *ii*) the directional phases of [25], [30], where the element phases were

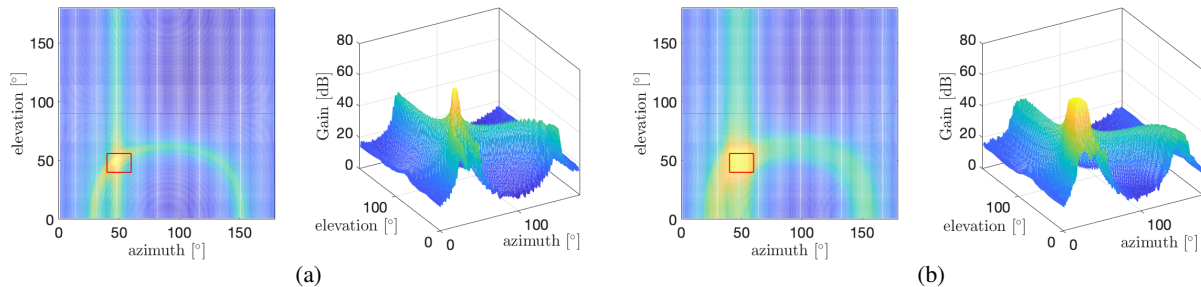


Fig. 5: The gain $\sum_{t=1}^{20} |G_t(\phi)|^2$ in dB for exemplary beampatterns of a 2D RIS using: (a) directional phase profiles; and (b) the proposed uniform phase profile in Section III-B. The red squares at left of each subfigure demonstrate the angular uncertainty that needs to be illuminated with sufficient beamforming gain.

sampled from the Gaussian angular uncertainty. It is noted that the CRLBs of the UE state were obtained by only using the RIS path, due to the unknown data association between the measurements of the NRIS paths (i.e., the uncontrolled ones) and landmarks, loosening the gap between the CRLBs and the performance of the proposed estimation approach.

1) *Beampattern Gain*: Even though the directional RIS phase profiles provide performance improvements over the random ones [25], [30], the possibility that a directional beam cannot provide sufficient gain increases as the uncertainty of the UE position prior increases. This happens due to the narrow beam width and the limited number of transmissions. To assess the beam quality, we define the following metric that quantifies the total received power at the UE, due to the RIS reflection, with a given RIS phase profile over T transmission intervals: $G \triangleq \sum_{t=1}^T |G_t(\phi_k)|^2$, where $G_t(\phi_k) = \omega_{t,k}^\top \mathbf{b}(\phi_k)$.

Aiming to cover the highlighted UE angular uncertainty region spanning onto $[40^\circ, 60^\circ]$ in the azimuth and $[-60^\circ, 40^\circ]$ in the elevation, Fig. 4 considers a $T = 5$ transmission interval and illustrates the beampatterns of a 2D RIS in the azimuth domain (Fig. 4a– 4c) with the fixed elevation $\phi_0^{\text{el}} = -50^\circ$, and in the elevation domain (Fig. 4d– 4f) with the fixed azimuth $\phi_0^{\text{az}} = 50^\circ$. The beampatterns are visualized for the directional phases (Fig. 4a and 4d), the optimized beam design of [39] (Fig. 4b and 4e), and the proposed adaptive beams in Section III-B (Fig. 4c and 4f). As it can be seen from the resulting sharp beams, the directional phases cannot uniformly illuminate the desired angular sector, and thus, the UE cannot be provided with a sufficient gain if it lies close to the edges of the uncertainty region. The RIS phase optimization in [39] enables generating beampatterns that are similar to rectangular pulse shapes, where the gain over the desired angular sector is maximized. In this case, a resulting gain of more than 20 dB is

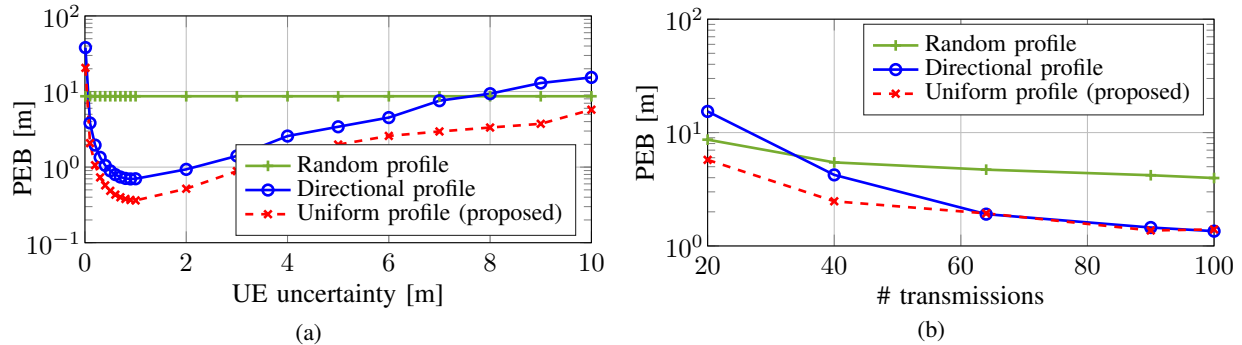


Fig. 6: PEBs on the UE state as function of (a) the UE uncertainties in meters for $T = 20$ transmission intervals; and (b) the number of transmission intervals for the case where the UE position uncertainty is 10 m.

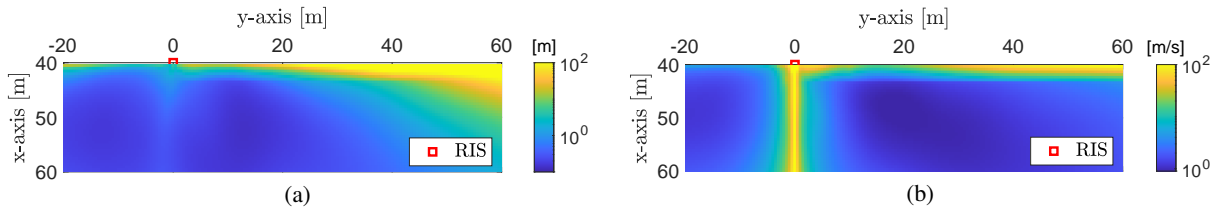


Fig. 7: Visualization of the (a) PEB and (b) SEB with different UE positions, using only the RIS path and $T = 20$ transmission intervals. The UE position uncertainty was set to 1 m.

achievable within the desired sector. However, it comes at the cost of increased computational complexity due to the required iterative optimization. On the other hand, the proposed RIS phase configurations enable uniform illumination of the uncertainty angular region in a more efficient way than the approach in [39], in terms of achievable power gain and computational complexity. This happens because it is relatively harder to find the global optimum point as the UE prior is larger. Finally, Fig. 5 includes the visualization of the sum of beampatterns over $T = 20$ transmissions, as generated by the directional phases (Fig. 5a) and the proposed ones (Fig. 5b). The desired angular sector is marked by red squares in the left subfigures in Figs. 5a and 5b. The results confirm that the entire angular sector can be illuminated by the proposed phase profiles with sufficient power; this does not happen, however, using the directional profiles.

2) *UE State Error Bounds:* The position error bound (PEB), heading error bound (HEB), and speed error bound (SEB) are henceforth evaluated over prior uncertainties, different UE positions, and numbers of transmissions.

a) *Impact of Prior Uncertainties:* The PEB performance versus the UE position prior uncertainties is plotted in Fig. 6a, using the CRLBs on the UE state, as derived in Appendix B. We have omitted the HEB and SEB, which tended to be similar to the PEB. It is obvious from

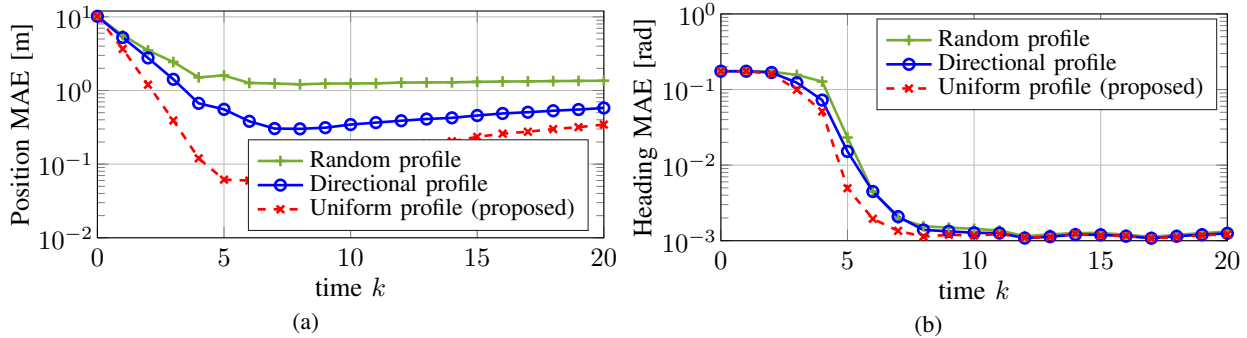


Fig. 8: Localization performance versus the time steps for $T = 20$ transmission intervals: MAEs of the (a) position; and (b) heading estimates.

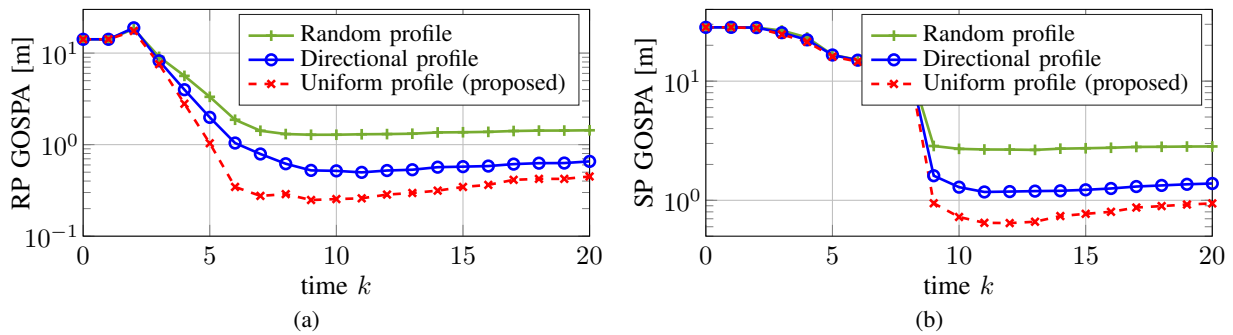


Fig. 9: Mapping performance for $T = 20$ transmission intervals: GOSPA distances of the (a) RP and (b) SP.

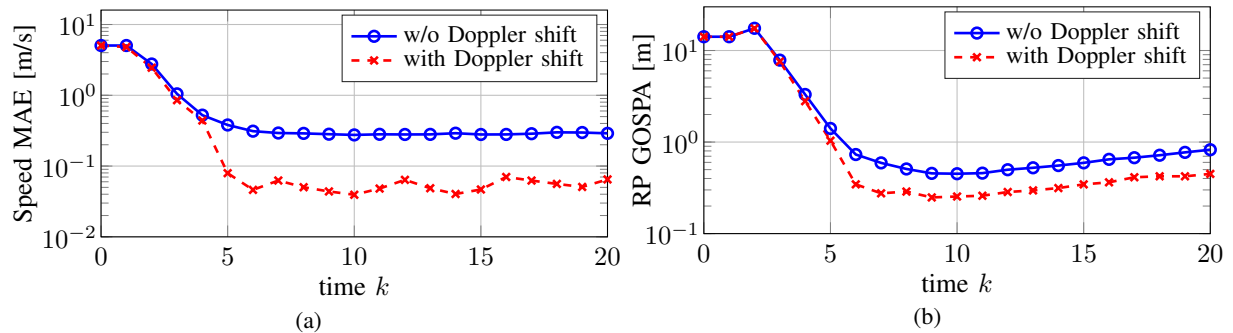


Fig. 10: SLAM performance using the proposed RIS phase profile with and without Doppler shift: (a) MAE of the speed estimates; and (b) GOSPA distances of the RP using the proposed RIS phase profile for $T = 20$ transmission intervals.

the figure that, as the prior uncertainty increases, the PEBs for the proposed uniform phases and the directional ones increase, while the random phases do not depend on the uncertainty. In addition, the gain of the proposed method gradually increases. This happens because when the UE uncertainty becomes large, the probability that the UE gets illuminated using RIS-controlled signals, and thus provided with sufficient received signal power, decreases. However, the PEB also increases when the UE uncertainty becomes smaller than 1 m, due to the lack of direction diversity. It can be also seen in the figure that the PEB offered by the directional phases is larger

than that when random phases are used, when the UE uncertainty is larger than 8 m.

b) Impact of the Number of Transmissions: The PEB performance as a function of the number of transmissions T is depicted in Fig. 6b for the case where the UE uncertainty is 10 m ($\bar{\mathbf{P}}_0 = \text{diag}(50, 50, 0)$). We have omitted the HEB and SEB performances, which were shown to have the same trend with PEB. It can be seen that, as T increases during the coherence time, the PEBs for all considered methods decreases. It is shown that the gain of the proposed method gradually decreases compared to the benchmarks. In all transmissions, the error bounds (EBs) of the proposed phase profiles are better than the random ones, and similar to, or slightly better than, the directional ones. This happens because, as T increases, the angular uncertainty, that is not illuminated, gradually decreases. When $T = 20$, the EBs of the directional phases are worse than that with random phases, but this trend gets reversed for $T > 40$.

c) Impact of the UE Positions: We visualize the PEB and SEB performances for different UE positions in the xy plane in Fig. 7. We have omitted the HEB, which was found to be similar to the PEB. We can see that the EBs become usually larger when the UE position is further away from the RIS. The PEB and SEB at about $x = 40$ m are relatively larger than other positions, because the RIS elements lie in the yz plane heading to $\mathbf{n}_{\text{RIS}} = [1, 0, 0]^\top$. The SEB at about $y = 0$ m is extremely larger than the other positions, since in this case, the UE velocity vector is orthogonal to the radial direction from the RIS to the UE, meaning that Doppler measurements provide no information on the longitudinal speed.

C. SLAM Performance

We next investigate the SLAM performance over time for the proposed modified MPMB-SLAM filter presented in Section IV, using the proposed RIS phase profile design in Section III-B.

1) The Role of the Phase Profile: The MAEs of the UE position, heading, and speed estimates over the discrete time index k are illustrated in Fig. 8. As shown, the MAEs of the estimates increase after $k = 8$, while the gain of the proposed uniform phase profile decreases when compared with the benchmarked ones. This happens because the UE moves, getting close to the RIS until $k = 8$, and far away from it after this time instant. It is also depicted that the localization performance with the directional phase profiles (i.e., the conventional and proposed ones) is always better than that with random phases. We omit the SEB, which was found to be similar to the HEB. The averaged mapping GOSPA distances for the RP and SPs are depicted in Fig. 9. It

is confirmed that the proposed framework with the NRIS paths can well estimate the landmark positions and classify the landmark types, while being robust to the missed detections and false alarms. Due to the correlation between the UE and landmarks in the geometric parameters, the mapping performance gain tends to be similar to the PEB, even though the RIS phase profile design never affects the FIM of the NRIS paths, which have been set to be uncontrollable.

2) *Impact of the Doppler Shift:* We next present results of Doppler-assisted SLAM, where the Doppler shift is used as an additional measurement in the update step of the proposed SLAM filter. To showcase the efficiency of the Doppler consideration in SLAM, the performance without the Doppler measurement is used as benchmark, and thus, evaluated.

The MAE of the speed estimates is illustrated in Fig. 10a, while the MAEs of the heading and position estimates were similar and omitted. It is depicted that, thanks to the Doppler shift measurement, the speed estimate is improving. Consequently, it is turned into a benefit in both position and heading estimates. The GOSPA distances of the RP are demonstrated in Fig. 10b; the GOSPA distances of SPs were similar, and thus, omitted. As before, it is shown that there is a performance improvement in the mapping with the Doppler shift estimate. Due to the large error of the UE speed estimates without the Doppler estimate, the potential landmarks (that have not been detected or have been detected with low existence probabilities) are located at errant positions. This causes frequent errors in data association, such that RPs measurements are associated with SPs, leading to false alarms in the RP mapping. Inevitably, there are missed detections in the SP mapping; the potentially true SPs cannot be associated with the SP measurements, due to the latter data association error.

VI. CONCLUSIONS

In this paper, we presented a novel RIS-enabled radio SLAM framework, considering a multi-antenna UE, a passive reflective RIS, a large surface, scattering points, and no BSs. An efficient method for RIS phase profile design, which can uniformly illuminate any desired angular sector where the UE is probabilistically located, was designed. We have also derived the CRLB of the channel parameters and the UE state, using only the RIS-induced path. According to the proposed online framework, the RIS phase design and the SLAM filter are recursively designed over time. We evaluated the proposed SLAM approach in the considered propagation environment with respect to different UE uncertainties and positions, number of transmissions, as well as with/without Doppler shift. Our results demonstrated that the proposed RIS phase profile

outperforms directional and random reflective beams, in terms of the RIS-based power gain for wireless communications, as well as in terms of localization and mapping accuracy for SLAM. It was also showcased that the proposed RIS profiles and modified MPMB-SLAM filter including Doppler shift estimation yield improved estimation performance.

For future work, we intend to study sensing and SLAM aided by RISs for integrated sensing, localization, and communications. The availability of prior SLAM information will be exploited for beamforming and combining designs that can recursively improve the sensing and localization performance over time. In addition, we will study near-field propagation environments aided by extremely large RIS in THz frequency band. We will finally investigate practical hardware impairments in RIS-aided sensing, SLAM, and communications.

APPENDIX A

GEOMETRY RELATIONS OF THE CHANNEL PARAMETERS

In this appendix, we define the geometry relations of the parameters for each channel path l . For notation simplicity, we omit the time index k and the transmission index t . We denote the location of the incident point for l -th path by \mathbf{x}_l , which is defined as $\mathbf{x}_l = \mathbf{x}_{\text{RIS}}$ for $l = 0$ and $\mathbf{x}_l = \mathbf{x}_{\text{IP}}^{(m)}$ for $l \neq 0$, where $\mathbf{x}_{\text{IP}}^{(\text{SP})} = \mathbf{x}^{(\text{SP})}$ and $\mathbf{x}_{\text{IP}}^{(\text{RP})} = \mathbf{x}^{(\text{RP})}$.

The Doppler shift is defined as⁸ $f_l^{\text{D}} = 2f_c v_l / c$, where v_l denotes the relative radial velocity to the landmark corresponding to⁹ path l . The channel parameters are defined as:

$$v_l = \begin{cases} \mathbf{v}_{\text{UE}}^{\top} \mathbf{x}_{\text{RU}} / d_{\text{RU}}, & l = 0 \\ \mathbf{v}_{\text{UE}}^{\top} \mathbf{x}_{\text{IU}}^{(m)} / d_{\text{IU}}^{(m)}, & l \neq 0 \end{cases}, \quad \phi^{\text{az}} = \text{atan2}(\check{y}_{\text{UR}}, \check{x}_{\text{UR}}), \quad \phi^{\text{el}} = \text{acos}(\check{z}_{\text{UR}} / d_{\text{UR}}),$$

$$\theta_l^{\text{az}} = \begin{cases} \text{atan2}(\check{y}_{\text{RU}}, \check{x}_{\text{RU}}), & l = 0 \\ \text{atan2}(\check{y}_{\text{IU}}, \check{x}_{\text{IU}}), & l \neq 0 \end{cases}, \quad \theta_l^{\text{el}} = \begin{cases} \text{acos}(\check{z}_{\text{RU}} / d_{\text{RU}}), & l = 0 \\ \text{acos}(\check{z}_{\text{IU}} / d_{\text{IU}}), & l \neq 0 \end{cases}, \quad \tau_l = \begin{cases} 2d_{\text{UR}}, & l = 0 \\ 2d_{\text{IU}}, & l \neq 0 \end{cases},$$

where $\check{\mathbf{x}}_{\text{RU}} = [\check{x}_{\text{RU}}, \check{y}_{\text{RU}}, \check{z}_{\text{RU}}]^{\top} = \mathbf{O}_{\text{UE}}^{\top} \mathbf{x}_{\text{RU}}$, $\check{\mathbf{x}}_{\text{UR}} = [\check{x}_{\text{UR}}, \check{y}_{\text{UR}}, \check{z}_{\text{UR}}]^{\top} = \mathbf{O}_{\text{RIS}}^{\top} \mathbf{x}_{\text{UR}}$, $\mathbf{x}_{\text{RU}} = \mathbf{x}_{\text{RIS}} - \mathbf{x}_{\text{UE}}$, $\mathbf{x}_{\text{UR}} = \mathbf{x}_{\text{UE}} - \mathbf{x}_{\text{RIS}}$, $d_{\text{RU}} = d_{\text{UR}} = \|\mathbf{x}_{\text{UR}}\| = \|\check{\mathbf{x}}_{\text{UR}}\| = \|\mathbf{x}_{\text{RU}}\| = \|\check{\mathbf{x}}_{\text{RU}}\|$, $\mathbf{x}_{\text{IU}}^{(m)} = \mathbf{x}_{\text{IP}}^{(m)} -$

⁸The Doppler shift is generally given by $f^{\text{D}} = f_c \Delta v / c$ with Δv denoting the relative velocity of the receiver to the transmitter. For example, let us suppose that the UE moves to a landmark at its speed v . Then, the UE radial velocity and the landmark radial velocity viewed by the UE, are respectively v and $-v$, and it holds $\Delta v = 2v$.

⁹We define the radial velocity v_l as the scalar projection of the velocity vector \mathbf{v}_{UE} onto \mathbf{e}_l , i.e., $v_l = \mathbf{v}_{\text{UE}}^{\top} \mathbf{e}_l$, where $\mathbf{v}_{\text{UE}} \triangleq [v_{\text{UE}} \cos \alpha_{\text{UE}}, v_{\text{UE}} \sin \alpha_{\text{UE}}, 0]^{\top}$ denotes the UE velocity vector in the Cartesian coordinate system and $\mathbf{e}_l \triangleq (\mathbf{x}_l - \mathbf{x}_{\text{UE}}) / \|\mathbf{x}_l - \mathbf{x}_{\text{UE}}\|$ is the unit-vector from the UE location \mathbf{x}_{UE} to the object \mathbf{x}_l . Note that \mathbf{v}_{UE} is represented by the UE heading and speed in the polar coordinate system.

\mathbf{x}_{UE} , and $d_{\text{IU}}^{(m)} = \|\mathbf{x}_{\text{IU}}^{(m)}\|$. In the latter definitions, $\mathbf{O}_{\text{RIS}} = [\mathbf{o}_{\text{RIS},1}, \mathbf{o}_{\text{RIS},2}, \mathbf{o}_{\text{RIS},3}]$ and $\mathbf{O}_{\text{UE}} = [\mathbf{o}_{\text{UE},1}, \mathbf{o}_{\text{UE},2}, \mathbf{o}_{\text{UE},3}]$. By denoting the real and imaginary parts as β_l^{Re} and β_l^{Im} , respectively, the complex channel gain of each l -th path is defined as follows: $\beta_l = \beta_l^{\text{Re}} + j\beta_l^{\text{Im}}$.

APPENDIX B

FISHER INFORMATION MATRIX OF THE CHANNEL PARAMETERS AND UE STATE

We describe the FIM derivation, providing the lower bounds on the estimation error of any unbiased estimator. We next present the FIM of the channel parameters for $l = 0, \dots, L$, given the received signal of (1). We also derive the FIM of the UE state from the FIM of the channel parameters corresponding to the RIS path, leveraging the variable transformation from the equivalent FIM (EFIM) of the channel parameters for the RIS path. This holds due to the considered time-domain RIS phase profiles, which enable separation of the RIS path ($l = 0$) from the other NRIS paths (i.e., $\forall l \neq 0$) without any data association process, as discussed in Section III-A1. For notational simplicity, we omit the time index k in the following.

A. FIM of the Channel Parameters

We introduce the channel parameter vector notation $\bar{\boldsymbol{\eta}} \triangleq [\tilde{\boldsymbol{\eta}}^\top, (\boldsymbol{\beta}^{\text{Re}})^\top, (\boldsymbol{\beta}^{\text{Im}})^\top]^\top$, where $\tilde{\boldsymbol{\eta}} = [\boldsymbol{\phi}_0^\top, \boldsymbol{\tau}^\top, \mathbf{v}^\top, \boldsymbol{\theta}^\top]^\top$ with $\boldsymbol{\tau} = [\tau_0, \dots, \tau_L]^\top$, $\mathbf{v} = [v_0, \dots, v_L]^\top$, and $\boldsymbol{\theta} = [\boldsymbol{\theta}_0^\top, \dots, \boldsymbol{\theta}_L^\top]^\top$, $\boldsymbol{\beta}^{\text{Re}} = [\beta_0^{\text{Re}}, \dots, \beta_L^{\text{Re}}]^\top$, and $\boldsymbol{\beta}^{\text{Im}} = [\beta_0^{\text{Im}}, \dots, \beta_L^{\text{Im}}]^\top$. We also represent the noiseless part of the received signal in (1) by $\bar{y}_{t,s}$ and we define $\bar{\mathbf{y}}_t \triangleq [\bar{y}_{t,1}, \dots, \bar{y}_{t,N_{\text{SC}}}]^\top$ including all N_{SC} subcarriers. Using the latter definitions, the FIM of the channel parameters can be computed as follows [63]:

$$\mathbf{J}(\bar{\boldsymbol{\eta}}) = \frac{2E_s}{N_0} \sum_{t=0}^T \text{Re} \left\{ \left(\frac{\partial \bar{\mathbf{y}}_t}{\partial \bar{\boldsymbol{\eta}}_k} \right)^{\text{H}} \frac{\partial \bar{\mathbf{y}}_t}{\partial \bar{\boldsymbol{\eta}}} \right\}, \quad (19)$$

where $\text{Re}\{\cdot\}$ is the function for extracting the real part of a complex number, $\partial/\partial\boldsymbol{\lambda}$ indicates the partial derivative with respect to the channel parameters (such as ToAs, radial velocities, AoDs, and path gains), and $\mathbf{J}(\bar{\boldsymbol{\eta}}) \in \mathbb{R}^{(2+6(L+1)) \times (2+6(L+1))}$ is of the following form:

$$\mathbf{J}(\bar{\boldsymbol{\eta}}) = \begin{bmatrix} \langle \mathbf{J}(\bar{\boldsymbol{\eta}}) \rangle_{11} & \langle \mathbf{J}(\bar{\boldsymbol{\eta}}) \rangle_{12} \\ \langle \mathbf{J}(\bar{\boldsymbol{\eta}}) \rangle_{12}^\top & \langle \mathbf{J}(\bar{\boldsymbol{\eta}}) \rangle_{22} \end{bmatrix}, \quad (20)$$

$$\langle \mathbf{J}(\bar{\boldsymbol{\eta}}) \rangle_{11} \in \mathbb{R}^{(2+4(L+1)) \times (2+4(L+1))}, \quad \langle \mathbf{J}(\bar{\boldsymbol{\eta}}) \rangle_{12} \in \mathbb{R}^{(2+4(L+1)) \times 2(L+1)}, \quad \langle \mathbf{J}(\bar{\boldsymbol{\eta}}) \rangle_{22} \in \mathbb{R}^{2(L+1) \times 2(L+1)}.$$

We also define $\tilde{\boldsymbol{\eta}}$ for the channel parameter vector $\bar{\boldsymbol{\eta}}$ when the channel coefficient $\boldsymbol{\beta}^{\text{Re}}$ and $\boldsymbol{\beta}^{\text{Im}}$ are excluded. To remove the effect of these nuisance parameters, we compute an EFIM as follows:

$\mathbf{J}(\tilde{\boldsymbol{\eta}}) = \langle \mathbf{J}(\tilde{\boldsymbol{\eta}}) \rangle_{11} - \langle \mathbf{J}(\tilde{\boldsymbol{\eta}}) \rangle_{12} \langle \mathbf{J}(\tilde{\boldsymbol{\eta}}) \rangle_{22}^{-1} \langle \mathbf{J}(\tilde{\boldsymbol{\eta}}) \rangle_{12}^\top$. To obtain the FIM of the channel parameters $\boldsymbol{\eta} = [\boldsymbol{\eta}_0^\top, \dots, \boldsymbol{\eta}_L^\top]^\top$ with $\boldsymbol{\eta}_0 = [\boldsymbol{\phi}^\top, \tau_0, v_0, \boldsymbol{\theta}_0^\top]^\top$ and $\boldsymbol{\eta}_l = [\tau_l, v_l, \boldsymbol{\theta}_l^\top]^\top$ for $l = 1, \dots, L$, we reorder the rows and columns of $\mathbf{J}(\tilde{\boldsymbol{\eta}}) \in \mathbb{R}^{(2+4(L+1)) \times (2+4(L+1))}$ and obtain $\mathbf{J}(\boldsymbol{\eta})$. The measurements noise covariance of (5) and (6) are then determined by extracting the sub-matrix $\mathbf{R}^j = \mathbf{J}^{-1}(\boldsymbol{\eta}_j)$ (corresponding to the channel parameters $\boldsymbol{\eta}_j$) for the measurement indices $j = 0, \dots, J$.

B. FIM of the UE State Using the RIS Path

Given the FIM expression $\mathbf{J}(\boldsymbol{\eta})$, we can compute an EFIM corresponding to $\boldsymbol{\eta}_0$ as follows:

$$\mathbf{J}(\boldsymbol{\eta}_0) = \langle \mathbf{J}(\boldsymbol{\eta}) \rangle_{11} - \langle \mathbf{J}(\boldsymbol{\eta}) \rangle_{12} \langle \mathbf{J}(\boldsymbol{\eta}) \rangle_{22}^{-1} \langle \mathbf{J}(\boldsymbol{\eta}) \rangle_{12}^\top, \quad (21)$$

where $\langle \mathbf{J}(\boldsymbol{\eta}) \rangle_{11} \in \mathbb{R}^{6 \times 6}$, $\langle \mathbf{J}(\boldsymbol{\eta}) \rangle_{12} \in \mathbb{R}^{6 \times 4L}$, and $\langle \mathbf{J}(\boldsymbol{\eta}) \rangle_{22} \in \mathbb{R}^{4L \times 4L}$. Finally, we calculate the FIM referring to the UE state \mathbf{s} by $\mathbf{J}(\mathbf{s}) = \mathbf{T}^\top \mathbf{J}(\boldsymbol{\eta}_0) \mathbf{T}$, where $\mathbf{T} \in \mathbb{R}^{6 \times 5}$ denotes the Jacobian transformation matrix, which is defined as $\mathbf{T} = \partial \boldsymbol{\eta}_0 / \partial \mathbf{s}$; the derivatives are detailed in the following Appendix C. The PEB, HEB, and SEB are finally given by

$$\text{PEB} = \sqrt{\text{tr}([\mathbf{J}^{-1}(\mathbf{s})]_{1:3,1:3})}, \quad \text{HEB} = \sqrt{[\mathbf{J}^{-1}(\mathbf{s})]_{4,4}}, \quad \text{SEB} = \sqrt{[\mathbf{J}^{-1}(\mathbf{s})]_{5,5}}. \quad (22)$$

APPENDIX C

THE JACOBIAN TRANSFORMATION MATRIX

The derivatives for the Jacobian transformation matrix \mathbf{T} are derived as follows:

$$\begin{aligned} \frac{\partial \phi^{\text{az}}}{\partial \mathbf{x}_{\text{UE}}} &= \frac{\check{x}_{\text{UR}} \mathbf{o}_{\text{RIS},2} - \check{y}_{\text{UR}} \mathbf{o}_{\text{RIS},1}}{\check{x}_{\text{UR}}^2 + \check{y}_{\text{UR}}^2}, & \frac{\partial \phi^{\text{el}}}{\partial \mathbf{x}_{\text{UE}}} &= \frac{1}{\sqrt{\check{x}_{\text{UR}}^2 + \check{y}_{\text{UR}}^2}} \left(\frac{\check{z}_{\text{UR}}}{d_{\text{UR}}^2} \mathbf{x}_{\text{UR}} - \mathbf{o}_{\text{RIS},3} \right), \\ \frac{\partial \theta_0^{\text{az}}}{\partial \mathbf{x}_{\text{UE}}} &= \frac{\check{y}_{\text{RU}} \mathbf{o}_{\text{UE},1} - \check{x}_{\text{RU}} \mathbf{o}_{\text{UE},2}}{\check{x}_{\text{RU}}^2 + \check{y}_{\text{RU}}^2}, & \frac{\partial \theta_0^{\text{el}}}{\partial \mathbf{x}_{\text{UE}}} &= \frac{1}{\sqrt{\check{x}_{\text{RU}}^2 + \check{y}_{\text{RU}}^2}} \left(\mathbf{o}_{\text{UE},3} - \frac{\check{z}_{\text{RU}}}{d_{\text{RU}}^2} \mathbf{x}_{\text{RU}} \right), \\ \frac{\partial \tau_0}{\partial \mathbf{x}_{\text{UE}}} &= \frac{\mathbf{x}_{\text{UR}}}{d_{\text{UR}}}, & \frac{\partial v_0}{\partial \mathbf{x}_{\text{UE}}} &= \frac{v_0}{d_{\text{RU}}} \mathbf{x}_{\text{RU}} - \frac{1}{d_{\text{RU}}} \mathbf{v}_{\text{UE}}, \\ \frac{\partial \theta_0^{\text{az}}}{\partial \alpha_{\text{UE}}} &= \frac{-(\check{x}_{\text{RU}} \mathbf{o}_{\text{UE},1}^\top + \check{y}_{\text{RU}} \mathbf{o}_{\text{UE},2}^\top) \mathbf{x}_{\text{RU}}}{\check{x}_{\text{RU}}^2 + \check{y}_{\text{RU}}^2}, & \frac{\partial \theta_0^{\text{el}}}{\partial \alpha_{\text{UE}}} &= 0, \\ \frac{\partial v_0}{\partial \alpha_{\text{UE}}} &= \frac{-v_{\text{UE}} \sin \alpha_{\text{UE}} x_{\text{RU}} + v_{\text{UE}} \cos \alpha_{\text{UE}} y_{\text{RU}}}{d_{\text{RU}}}, & \frac{\partial v_0}{\partial v_{\text{UE}}} &= \frac{1}{d_{\text{RU}}} (x_{\text{RU}} \cos \alpha_{\text{UE}} + y_{\text{RU}} \sin \alpha_{\text{UE}}). \end{aligned}$$

REFERENCES

- [1] H. Kim, K. Granström, L. Gao *et al.*, “5G mmWave cooperative positioning and mapping using multi-model PHD,” *IEEE Trans. Wireless Commun.*, vol. 19, no. 6, pp. 3782–3795, Mar. 2020.
- [2] Y. Ge, O. Kaltiokallio, H. Kim *et al.*, “A computationally efficient EK-PMBM filter for bistatic mmWave radio SLAM,” *IEEE J. Sel. Areas Commun.*, vol. 40, no. 7, Jul. 2022.

- [3] H. Kim, K. Granstrom, L. Svensson *et al.*, “PMBM-based SLAM filters in 5G mmWave vehicular networks,” *IEEE Trans. Veh. Technol.*, vol. 71, no. 8, pp. 8646–8661, Aug. 2022.
- [4] H. Wymeersch, N. Garcia, H. Kim *et al.*, “5G mmWave downlink vehicular positioning,” in *Proc. IEEE Global Commun. Conf. (GLOBECOM)*, Abu Dhabi, UAE, Dec. 2018, pp. 206–212.
- [5] H. Kim, H. Wymeersch, N. Garcia *et al.*, “5G mmWave vehicular tracking,” in *Proc. IEEE 52nd Asilomar Conf. Signals, Syst., Comput.*, Pacific Grove, CA, USA, Oct. 2018, pp. 541–547.
- [6] E. Leitinger, F. Meyer, F. Hlawatsch *et al.*, “A belief propagation algorithm for multipath-based SLAM,” *IEEE Trans. Wireless Commun.*, vol. 18, no. 12, pp. 5613–5629, Sep. 2019.
- [7] R. Mendrzik, F. Meyer, G. Bauch *et al.*, “Enabling situational awareness in millimeter wave massive MIMO systems,” *IEEE J. Sel. Topics Signal Process.*, vol. 13, no. 5, pp. 1196–1211, Aug. 2019.
- [8] A. Yassin, Y. Nasser, A. Y. Al-Dubai *et al.*, “MOSAIC: Simultaneous localization and environment mapping using mmWave without a-priori knowledge,” *IEEE Access*, vol. 6, pp. 68 932–68 947, Nov. 2018.
- [9] J. Palacios, G. Bielsa, P. Casaril *et al.*, “Communication-driven localization and mapping for millimeter wave networks,” in *Proc. IEEE Int. Conf. Comput. Commun. (INFOCOM)*, Honolulu, HI, USA, Apr. 2018, pp. 2402–2410.
- [10] H. Durrant-Whyte and T. Bailey, “Simultaneous localization and mapping: Part I,” *IEEE Robot. Autom. Mag.*, vol. 13, no. 2, pp. 99–110, Jun. 2006.
- [11] T. Bailey and H. Durrant-Whyte, “Simultaneous localization and mapping (SLAM): Part II,” *IEEE Robot. Autom. Mag.*, vol. 13, no. 3, pp. 108–117, Sep. 2006.
- [12] R. D. Taranto, S. Muppirisetty, R. Raulefs *et al.*, “Location-aware communications for 5G networks: How location information can improve scalability, latency, and robustness of 5G,” *IEEE Signal Process. Mag.*, vol. 31, no. 6, pp. 102–112, Nov. 2014.
- [13] M. Koivisto, A. Hakkarainen, M. Costa *et al.*, “High-efficiency device positioning and location-aware communications in dense 5G networks,” *IEEE Commun. Mag.*, vol. 55, no. 8, pp. 188–195, Aug. 2017.
- [14] A. Liu, Z. Huang, M. Li *et al.*, “A survey on fundamental limits of integrated sensing and communication,” *IEEE Commun. Surv. Tutor.*, vol. 24, no. 2, pp. 994–1034, 2nd Quart. 2022.
- [15] F. Liu, Y. Cui, C. Masouros *et al.*, “Integrated sensing and communications: Towards dual-functional wireless networks for 6G and beyond,” *IEEE journal on selected areas in communications*, Jun. 2022.
- [16] S. P. Chepuri, N. Shlezinger, F. Liu *et al.*, “Integrated sensing and communications with reconfigurable intelligent surfaces,” *arXiv preprint arXiv:2211.01003*, 2022.
- [17] G. C. Alexandropoulos, A. Mokh, R. Khayatzadeh *et al.*, “Time reversal for 6G wireless communications: Novel experiments, opportunities, and challenges,” *IEEE Veh. Technol. Mag.*, early access, 2022.
- [18] C. Huang, A. Zappone, G. C. Alexandropoulos *et al.*, “Reconfigurable intelligent surfaces for energy efficiency in wireless communication,” *IEEE Trans. Wireless Commun.*, vol. 18, no. 8, pp. 4157–4170, Aug. 2019.
- [19] M. Jian, G. C. Alexandropoulos, E. Basar *et al.*, “Reconfigurable intelligent surfaces for wireless communications: Overview of hardware designs, channel models, and estimation techniques,” *Intell. Converged Netw.*, vol. 3, no. 1, pp. 1–32, Mar. 2022.
- [20] E. Björnson, H. Wymeersch, B. Matthiesen *et al.*, “Reconfigurable intelligent surfaces: A signal processing perspective with wireless applications,” *IEEE Signal Process. Mag.*, vol. 39, no. 2, pp. 135–158, Mar. 2022.
- [21] E. Calvanese Strinati, G. C. Alexandropoulos, H. Wymeersch *et al.*, “Reconfigurable, intelligent, and sustainable wireless environments for 6G smart connectivity,” *IEEE Commun. Mag.*, vol. 59, no. 10, pp. 99–105, Oct. 2021.
- [22] H. Wymeersch, J. He, B. Denis *et al.*, “Radio localization and mapping with reconfigurable intelligent surfaces: Challenges, opportunities, and research directions,” *IEEE Veh. Technol. Mag.*, vol. 15, no. 4, pp. 52–61, 2020.

- [23] H. Zhang, B. Di, K. Bian *et al.*, “Toward ubiquitous sensing and localization with reconfigurable intelligent surfaces,” *Proc. IEEE*, vol. 110, no. 9, pp. 1401–1422, Sept. 2022.
- [24] K. Keykhosravi, B. Denis, G. C. Alexandropoulos *et al.*, “Leveraging RIS-enabled smart signal propagation for solving infeasible localization problems,” *arXiv preprint arXiv:2204.11538*, 2022.
- [25] K. Keykhosravi, M. F. Keskin, G. Seco-Granados *et al.*, “RIS-Enabled SISO localization under user mobility and spatial-wideband effects,” *IEEE J. Sel. Topics Signal Process.*, vol. 16, no. 5, pp. 1125–1140, Aug. 2022.
- [26] A. Elzanaty, A. Guerra, F. Guidi *et al.*, “Reconfigurable intelligent surfaces for localization: Position and orientation error bounds,” *IEEE Trans. Signal Process.*, vol. 69, pp. 5386–5402, Aug. 2021.
- [27] H. Chen, H. Srieddeen, T. Ballal *et al.*, “A tutorial on terahertz-band localization for 6G communication systems,” *IEEE Commun. Surv. Tutor.*, 3rd Quart. 2022.
- [28] D. Dardari, N. Decarli, A. Guerra *et al.*, “LOS/NLOS near-field localization with a large reconfigurable intelligent surface,” *IEEE Trans. Wireless Commun.*, vol. 21, no. 6, pp. 4282–4294, Jun. 2022.
- [29] B. Teng, X. Yuan, R. Wang *et al.*, “Bayesian user localization and tracking for reconfigurable intelligent surface aided MIMO systems,” *IEEE J. Sel. Topics Signal Process.*, vol. 16, no. 5, pp. 1040–1054, 2022.
- [30] K. Keykhosravi, G. Seco-Granados, G. C. Alexandropoulos *et al.*, “RIS-enabled self-localization: Leveraging controllable reflections with zero access points,” in *Proc. IEEE Int. Conf. Commun. Workshops (ICC)*, Seoul, South Korea, May 2022.
- [31] A. Aubry, A. De Maio, and M. Rosamilia, “RIS-aided radar sensing in NLOS environment,” in *Proc. IEEE 8th International Workshop on Metrology for AeroSpace (MetroAeroSpace)*, Jun. 2021, pp. 277–282.
- [32] S. Buzzi, E. Grossi, M. Lops *et al.*, “RIS-aided monostatic MIMO radar with co-located antennas,” in *IEEE Int. Conf. Acoust., Speech, Signal Process. (ICASSP)*, May 2022, pp. 4998–5002.
- [33] R. Ghazalian, K. Keikhosravi, H. Chen *et al.*, “Bi-static sensing for near-field RIS localization,” *arXiv preprint arXiv:2206.13915*, 2022.
- [34] Z. Yang, H. Zhang, H. Zhang *et al.*, “MetaSLAM: Wireless simultaneous localization and mapping using reconfigurable intelligent surfaces,” *IEEE Trans. Wireless Commun.*, 2022.
- [35] Y. He, Y. Cai, H. Mao *et al.*, “RIS-assisted communication radar coexistence: Joint beamforming design and analysis,” *IEEE J. Sel. Areas Commun.*, Jul. 2022.
- [36] Z. Wang, Z. Liu, Y. Shen *et al.*, “Location awareness in beyond 5G networks via reconfigurable intelligent surfaces,” *IEEE J. Sel. Areas Commun.*, vol. 40, no. 7, pp. 2011–2025, Jul. 2022.
- [37] W. Wang and W. Zhang, “Joint beam training and positioning for intelligent reflecting surfaces assisted millimeter wave communications,” *IEEE Transactions on Wireless Communications*, vol. 20, no. 10, pp. 6282–6297, Oct. 2021.
- [38] A. Fascista, M. F. Keskin, A. Coluccia *et al.*, “RIS-aided joint localization and synchronization with a single-antenna receiver: Beamforming design and low-complexity estimation,” *IEEE J. Sel. Topics Signal Process.*, vol. 16, no. 5, pp. 1141–1156, Aug. 2022.
- [39] M. Rahal, B. Denis, K. Keykhosravi *et al.*, “Arbitrary beam pattern approximation via riss with measured element responses,” in *Joint European Conference on Networks and Communications & 6G Summit (EuCNC/6G Summit)*, Jun. 2022, pp. 506–511.
- [40] K. Meng, Q. Wu, R. Schober *et al.*, “Intelligent reflecting surface enabled multi-target sensing,” *IEEE Trans. Commun.*, 2022.
- [41] V. Jamali, G. C. Alexandropoulos, R. Schober *et al.*, “Low-to-zero-overhead irs reconfiguration: Decoupling illumination and channel estimation,” *IEEE Commun. Lett.*, vol. 26, no. 4, pp. 932–936, Apr. 2022.
- [42] G. C. Alexandropoulos, V. Jamali, R. Schober *et al.*, “Near-field hierarchical beam management for RIS-enabled millimeter

- wave multi-antenna systems,” in *IEEE Sensor Array and Multichannel Signal Processing Workshop*, Trondheim, Norway, Jun. 2022, pp. 1–5.
- [43] G. Noh, B. Hui, and I. Kim, “High speed train communications in 5G: design elements to mitigate the impact of very high mobility,” *IEEE Wireless Commun.*, vol. 27, no. 6, pp. 98–106, Dec. 2020.
- [44] Y. Han, Y. Shen, X.-P. Zhang *et al.*, “Performance limits and geometric properties of array localization,” *IEEE Trans. Inf. Theory*, vol. 62, no. 2, pp. 1054–1075, Dec. 2015.
- [45] A. Kakkavas, M. H. C. García, R. A. Stirling-Gallacher *et al.*, “Performance limits of single-anchor millimeter-wave positioning,” *IEEE Trans. Wireless Commun.*, vol. 18, no. 11, pp. 5196–5210, Aug. 2019.
- [46] H. Chen, F. Jiang, Y. Ge *et al.*, “Doppler-enabled single-antenna localization and mapping without synchronization,” *arXiv preprint arXiv:2205.15427*, 2022.
- [47] G. C. Alexandropoulos, M. A. Islam, and B. Smida, “Full-duplex massive multiple-input, multiple-output architectures: Recent advances, applications, and future directions,” *IEEE Vehicular Technology Magazine*, pp. 2–10, 2022.
- [48] X. R. Li and V. P. Jilkov, “Survey of maneuvering target tracking. Part I. Dynamic models,” *IEEE Trans. Aero. Electron. Syst.*, vol. 39, no. 4, pp. 1333–1364, Oct. 2003.
- [49] R. Mahler, *Statistical Multisource-Multitarget Information Fusion*. Norwood, MA, USA: Artech House, 2007.
- [50] F. Roemer, M. Haardt, and G. Del Galdo, “Analytical performance assessment of multi-dimensional matrix-and tensor-based ESPRIT-type algorithms,” *IEEE Trans. Signal Process.*, vol. 62, no. 10, pp. 2611–2625, May 2014.
- [51] F. Jiang, F. Wen, Y. Ge *et al.*, “Beamspace multidimensional ESPRIT approaches for simultaneous localization and communications,” *arXiv preprint arXiv:2111.07450*, 2021.
- [52] H. Wymeersch and G. Seco-Granados, “Adaptive detection probability for mmWave 5G SLAM,” in *6G Wireless Summit (6G SUMMIT)*, Mar. 2020.
- [53] Z. Abu-Shaban, K. Keykhosravi, M. F. Keskin *et al.*, “Near-field localization with a reconfigurable intelligent surface acting as lens,” in *ICC 2021 - IEEE International Conference on Communications*, 2021, pp. 1–6.
- [54] C. A. Balanis, *Antenna theory: analysis and design*. John Wiley & sons, 2015.
- [55] M. Slotani, “Tolerance regions for a multivariate normal population,” *Annals of the Institute of Statistical Mathematics*, vol. 16, no. 1, pp. 135–153, 1964.
- [56] Á. F. García-Fernández, J. L. Williams, K. Granström *et al.*, “Poisson multi-Bernoulli mixture filter: Direct derivation and implementation,” *IEEE Trans. Aerosp. Electron. Syst.*, vol. 54, no. 4, pp. 1883–1901, Aug. 2018.
- [57] J. L. Williams, “Marginal multi-Bernoulli filters: RFS derivation of MHT, JIPDA, and association-based MeMBer,” *IEEE Trans. Aerosp. Electron. Syst.*, vol. 51, no. 3, pp. 1664–1687, Jul. 2015.
- [58] K. G. Murty, “An algorithm for ranking all the assignments in order of increasing costs,” *Oper. Res.*, vol. 16, no. 3, pp. 682–687, 1968.
- [59] Z. Abu-Shaban, X. Zhou, T. Abhayapala *et al.*, “Error bounds for uplink and downlink 3D localization in 5G millimeter wave systems,” *IEEE Trans. Wireless Commun.*, vol. 17, no. 8, pp. 4939–4954, Aug. 2018.
- [60] S. W. Ellingson, “Path loss in reconfigurable intelligent surface-enabled channels,” in *Proc. IEEE Int. Symp. on Personal, Indoor and Mob. Radio Commun., (PIMRC)*, Sep. 2021, pp. 829–835.
- [61] I. Arasaratnam and S. Haykin, “Cubature Kalman filters,” *IEEE Trans. Autom. Control*, vol. 54, no. 6, pp. 1254–1269, Jun. 2009.
- [62] A. S. Rahmathullah, A. F. García Fernández, and L. Svensson, “Generalized optimal sub-pattern assignment metric,” in *Proc. 20th Int. Conf. Inf. Fusion (FUSION)*, Xian, China, Jul. 2017, pp. 1–8.
- [63] S. Kay, *Fundamentals of Statistical Signal Processing: Estimation Theory*. Prentice Hall Signal Processing Series, 1993.